Deformation and surface uplift associated with serpentinization at mid-ocean ridges and subduction zones

Leonid N. Germanovich,[1] Gence Genc,[1] Robert P. Lowell,[2] and Peter A. Rona[3]

Received 13 April 2012; revised 7 May 2012; accepted 8 May 2012; published 21 July 2012.

[1] We employ the classical problem of an inclusion in an elastic half-space to model effects of sub-surface serpentinization on crustal deformation, change of stress state, and surface uplift. At the TAG hydrothermal field on the Mid-Atlantic Ridge, the model suggests that an anomalous salient 3 km in diameter and 100 m high that projects 3.5 km westward from the east valley wall may have resulted from a relatively deep-seated well-serpentinized body exhibiting transformational strain. The associated large strains would likely result in sub-surface fracturing or faulting, but surface uplift may be relatively insensitive to the exact depth and shape of the serpentinized region. Serpentinization of a region beneath the footwall of the TAG detachment fault will tend to promote slip along some overlying normal faults, which may then enhance fluid pathways to the deeper crust to continue the serpentinization process. Our solution for the Miyazaki Plain above the Kyushu-Palau subduction zone in SW Japan explains the observed uplift of ≈120 m. The small transformational strains associated with serpentinization in this region may promote thrust-type events in the aseismic slip zone near the upper boundary of the subducting Philippine Sea Plate as well as intraplate earthquakes associated with normal faulting. The rate of serpentinization needed to produce the observed uplift at the Miyazaki Plain is significantly greater than that needed at TAG, though significantly smaller on per unit volume basis. Thermal effects of serpentinization in both regions appear to be small, but uplift data provide an additional constraint on inferring serpentinization from geological and seismological observations.

Citation: Germanovich, L. N., G. Genc, R. P. Lowell, and P. A. Rona (2012), Deformation and surface uplift associated with serpentinization at mid-ocean ridges and subduction zones, *J. Geophys. Res.*, *117*, B07103, doi:10.1029/2012JB009372.

1. Introduction

[2] Serpentinization is a term describing a number of exothermic olivine hydrolysis reactions that occur when seawater reacts with ultramafic rocks and the primary minerals olivine and pyroxene are replaced by serpentine [*Fyfe and Londsale*, 1981; *Macdonald and Fyfe*, 1985; *Allen and Seyfried*, 2004]. All of these reactions, which typically occur between 100 and 500°C [*Cannat et al.*, 1992; *Früh-Green et al.*, 1996; *Mével and Stamoudi*, 1996; *Agrinier et al.*, 1997], are exothermic releasing about 290 kJ/kg [*Fyfe and Londsale*, 1981; *Macdonald and Fyfe*, 1985]. In addition to releasing heat, serpentinization generally results in volume expansion ranging between 25% and 53% [*Coleman*, 1971; *O'Hanley*, 1992].

[3] Both geologic and geophysical data suggest that partially serpentinized peridotites and serpentinites are a significant part of the oceanic lithosphere especially that formed at slow-spreading ridges [e.g., *Rona et al.*, 1987; *Carlson and Miller*, 1997; *Escartin et al.*, 2001]. Serpentinization is observed in outcrops at ridge offsets, preferentially at inside corner highs [*Dick*, 1989; *Tucholke and Lin*, 1994; *Cannat et al.*, 1995], along ridge segments accreting with low magma supply [*Cannat et al.*, 1997; *Escartin and Cannat*, 1999], in upper mantle portions of ophiolites [*Bonatti*, 1976; *Bonatti and Hamlyn*, 1981; *Nicolas*, 1989; *Cannat*, 1993], and in cores recovered from shallow mantle of ocean ridges by the Ocean Drilling Program [*Gillis et al.*, 1993; *Früh-Green et al.*, 1996; *Karson and Lawrence*, 1997].

[4] Serpentinization is also important in other submarine settings such as rifted margins [e.g., *Reston*, 2009], the ocean-continent transition zone [e.g., *Skelton and Jakobsson*, 2007], and subduction zones [e.g., *Faccenda et al.*, 2008; *Tahara et al.*, 2008; *Hilairet and Reynard*, 2009]. The relationships between slow earthquakes and aseismic slip [*Hirauchi et al.*, 2010] and the serpentine mud volcanoes of the Mariana forearc, where fluids exsolved from the downgoing slab serpentinize the overlying mantle and ascend to

[1]School of Civil and Environmental Engineering, Georgia Institute of Technology, Atlanta, Georgia, USA.
[2]Department of Geosciences, Virginia Polytechnic Institute and State University, Blacksburg, Virginia, USA.
[3]Institute of Marine and Coastal Sciences and Department of Earth and Planetary Sciences, Rutgers University, New Brunswick, New Jersey, USA.

Corresponding author: R. P. Lowell, Department of Geosciences, Virginia Polytechnic Institute and State University, Blacksburg, VA 24061, USA. (rlowell@vt.edu)

0148-0227/12/2012JB009372

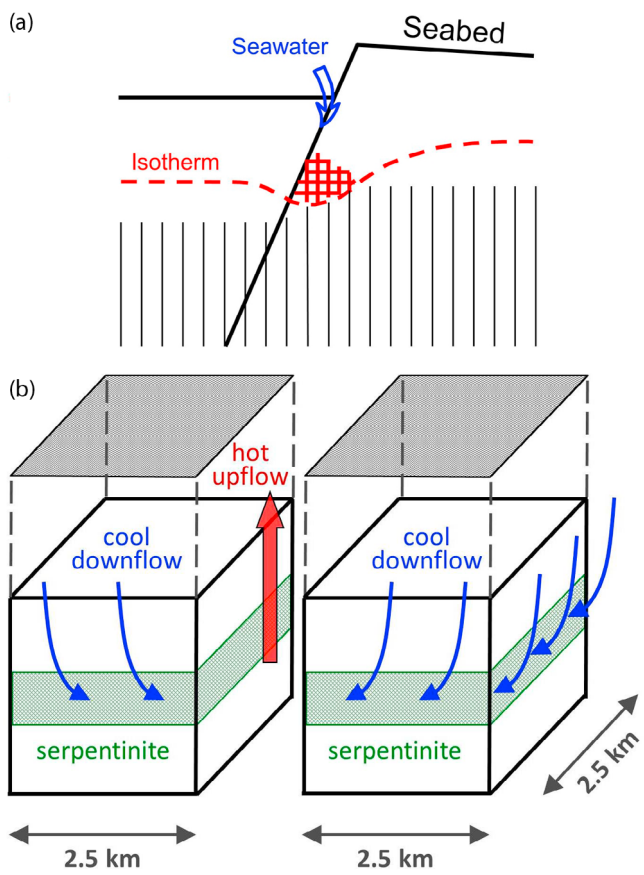

Figure 1. (a) Serpentinization at the footwall of a normal fault [after *Francis*, 1981]. Rocks beneath the footwall of a normal fault hydrate as a result of seawater infiltrating down the fault, so that serpentinization occurs generating more movement on the fault and uplift [*Francis*, 1981]. (b) Cartoon of 1-D uplift resulting from serpentinization of oceanic crust [after *Palmer*, 1996].

the surface through faults, are of particular interest in this context [e.g., *Fryer and Mottl*, 1992; *Fryer*, 1996a, 1996b; *Mottl et al.*, 2003; *Wheat et al.*, 2008].

[5] Mounting evidence indicates that serpentinization plays a role in structural deformation and uplift at mid-oceanic ridges where it is commonly associated with the formation of oceanic core complexes and detachment faults [e.g., *Francis*, 1981; *Zonenshain et al.*, 1989; *Bougault et al.*, 1993; *Cann et al.*, 1997; *Tucholke et al.*, 1998; *Escartin et al.*, 1997b, 2001; *Blackman et al.*, 2002; *Mével*, 2003; *Boschi et al.*, 2006; *Ildefonse et al.*, 2007; *MacLeod et al.*, 2009; *Miranda and Dilek*, 2010]. The connection between serpentinization and tectonics is complicated; however, some simple conceptual models exist. For example, *Dziak et al.* [2000], based on the interpretation of seismic data, suggested that the uplift of the Blanco Ridge is caused by serpentinized peridotite diapirs. *Francis* [1981] proposed the concept of serpentinization fault; that is, a fault triggered, induced, or affected by stress changes in a crustal region undergoing serpentinization and corresponding volumetric expansion. One of his scenarios, shown in Figure 1a, although not quantified, is partially consistent with the uplift observed at inside corner highs at ridge-transform intersections, though some of the uplift may be dynamically driven [*Tucholke and Lin*, 1994; *Tucholke et al.*, 1998].

[6] *Palmer* [1996] was among the first to develop a model of uplift assuming a characteristic volume expansion of 46% [*Coleman*, 1971; *O'Hanley*, 1992] of fully serpentinized peridotite and taking into account the changes in the density of oceanic crust. In his model, serpentinization occurs in a 1-D layer that expands causing the uplift. Although *Palmer*'s [1996] conclusion that the tectonics of slow-spreading ridges and their topography might result from serpentinization, in his 1-D model surface topography simply mimics the subsurface geometry of the serpentinized layer (Figure 1b).

[7] This model cannot be used to construct the 2-D features proposed by *Dziak et al.* [2000] or *Francis* [1981] (Figure 1a); or the more complex 3-D geomorphic features that might be attributed to subsurface serpentinization-driven deformations. For example, *Zonenshain et al.* [1989], investigating tectonics of the Mid-Atlantic ridge, suggested that the serpentinization leads not only to narrow serpentinized protrusions along fault planes, but also embraces relatively wide areas beneath the crust and induces uplift of large crustal blocks above the serpentinized layer. They argue that rift mountains and abnormal rift valley slopes are surface expressions that result from the serpentinization of mantle peridotite.

[8] As a particular case, a component of deformation at the TAG hydrothermal field may have been produced by volumetric expansion caused by serpentinization superimposed on a complex detachment fault structure. The central portion of the walls of the axial valley of spreading segments on slow-spreading ocean ridges is generally straight. In contrast, the central portion of the east wall of the axial valley, where some of the hydrothermal zones in the TAG field occur, exhibits an anomalous bulge about 6 km long between 26°08.0′N and 26°11.0′N that includes a salient centered at 26°08.3′N that projects about 3.5 km westward over the valley floor [*Rona et al.*, 1993] (Figure 2). The salient is bounded by the 3725 m (base) and 3625 m (top) isobaths and exhibits dome-shaped relief of about 100 m with a diameter of about 3000 m. *deMartin et al.* [2007] report two distinct clusters of microseismicity at depths of ~2–5 km below the seafloor with composite focal mechanisms consistent with normal faulting. One cluster conforms to the western edge of the bulge including the salient [*deMartin et al.*, 2007, Figure 1A]. The second cluster is aligned with the axial valley axis (23°N) where the bulge intersects the east wall. The eastern wall including the bulge is underlain at depths below 1 km by a high-velocity anomaly (seismic velocity exceeding 6.5 km/s), which according to *deMartin et al.* [2007], is indicative of "the presence of lower crustal and/or lower serpentinized upper mantle rocks at anomalously shallow depths." They report that the velocity anomaly dips westward toward the spreading axis at an angle of about 20° and passes under the active high-temperature TAG sulfide mound at a depth of ~1 km. They interpret these and related observations to support the existence of a major detachment fault in the east wall that projects up to ≈7 km downward [*deMartin et al.*, 2007]. The detachment fault may be a conduit for the flow of water into the upper mantle where serpentinization occurs. Boron levels in high-temperature hydrothermal fluids sampled from the TAG active sulfide mound (Figure 2) are lower than in seawater indicating ongoing uptake of boron

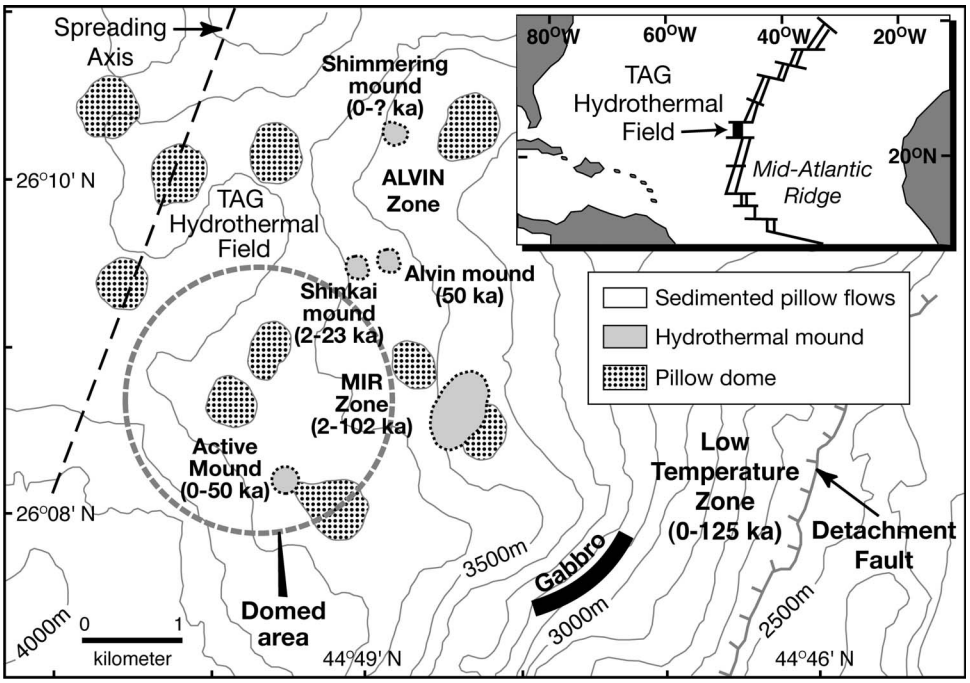

Figure 2. Bathymetric map of TAG hydrothermal field on the east wall of the axial valley of the Mid-Atlantic Ridge showing anomalous dome-shaped salient (encircled) centered near 26°08.7′N, 44°49.6′W with 100 m relief between 3725 m (base) and 3625 m (top) isobaths [modified from *Rona*, 2008]; the TAG field is inferred to lie on the hanging wall of a major detachment fault that crops out several kilometers to the east (lower right corner) [see also *deMartin et al.*, 2007, Figure 2].

by underlying serpentinization reactions [*Palmer*, 1996]. The salient and larger bulge may be a surface expression of deformation produced by a volume of serpentinized mantle located in the footwall beneath the hanging wall of the detachment fault [*Zonenshain et al.*, 1989; *Rona*, 2008]. In this paper, we develop a model showing that at least the anomalous salient in the east wall, if not the entire bulge, may be produced by expansion of an underlying volume of serpentinized mantle.

[9] Serpentinization of the mantle wedge near subduction zones [e.g., *Hyndman et al.*, 1997] can also result in deformation and uplift. For example, serpentinization of the mantle wedge near the subducted Kyushu-Palau Ridge may be related to the inferred regions of aseismic slip beneath the Kyushu region of Southwestern Japan [*Yagi and Kikuchi*, 2003] and to the crustal uplift of $\sim 10^2$ m of the overlying Miyazaki Plain during the past $\sim 1.2 \times 10^5$ years [*Nagaoka et al.*, 1991; *Tahara et al.*, 2008]. From seismic tomography data, *Tahara et al.* [2008] and *Saiga et al.* [2010] infer the existence of a region of low seismic velocity and high Poisson's ratio (Figures 3a and 3b) that may be associated with serpentinization near the subducted Kyushu-Palau Ridge. *Saiga et al.* [2010] depict this region as a quasi-elliptical inclined domain at a depth of 20–40 km beneath the Miyazaki Plain (Figure 3b). In addition, they show another sub-horizontal, quasi-elliptical region of low seismic velocity and near-normal Poisson's ratio (Figure 3b). Both *Tahara et al.* [2008] and *Saiga et al.* [2010] hypothesized that this sub-horizontal region denotes a zone of low-density buoyant material associated with subduction of the Kyushu-Palau Ridge, which may contribute to uplift of Kyushu Mountains. *Tahara et al.* [2008] proposed a similar mechanism for the Quaternary uplift of the Miyazaki Plain. In principal, buoyancy associated with a relatively low density of serpentinized material may certainly contribute to the crustal uplift, but we suggest that volume expansion resulting from incremental serpentinization of both of these regions could also result in the observed uplift of the Miyazaki Plain and Kyushu Mountains.

[10] The 2-D and 3-D deformations described above that may result from serpentinization beneath the seafloor will also lead to large strains in the neighborhood of region undergoing serpentinization. Such large strains are likely to result in faulting or tensile fracturing that would be difficult to account for in the 1-D model developed by *Palmer* [1996]. Moreover, these processes are likely to be important for promoting the serpentinization process by creating new permeability and allowing fluid access to fresh peridotite. To explore these issues, we consider a first-order model of crustal deformation and seafloor uplift resulting from volume expansion associated with the subsurface serpentinization. We employ a classic problem of an inclusion undergoing transformation strain in an elastic half-space. For simplicity, we assume that the transformation strain does not change elastic moduli in the inclusion. Using solutions of such problems for inclusions of different shapes, orientations and depths, we calculate the seafloor uplift. We discuss the topographic features at the TAG hydrothermal field and uplift of the Miyazaki Plain and Kyushu Mountains as examples.

[11] The importance of our analyses stems from treating the stress and strain effects resulting from serpentinization

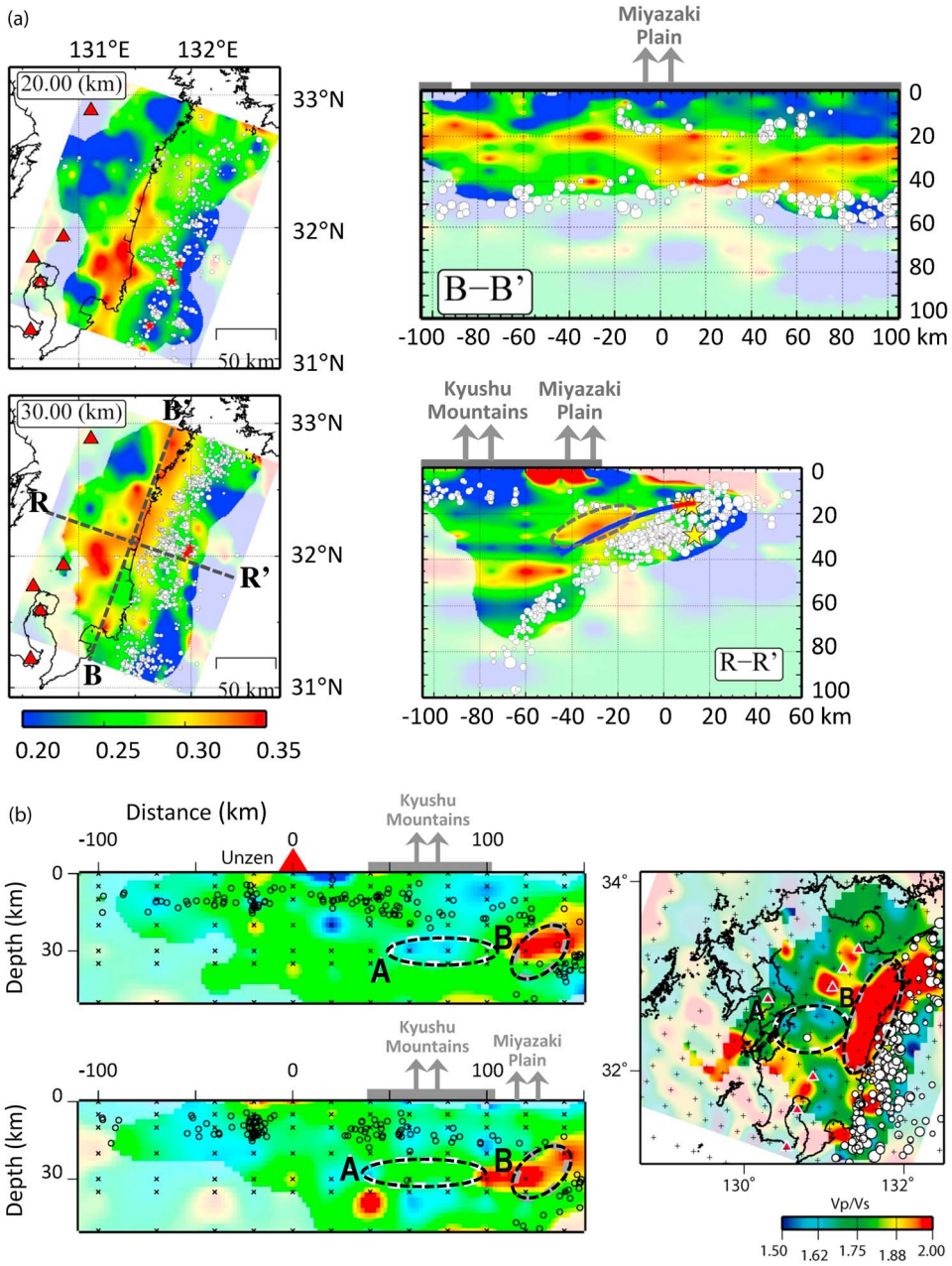

Figure 3. (a) Kyushu island (black coastline) and Poisson's ratio distribution at the depth of 20 km and 30 km (left), vertical cross-section underneath the line of B-B′ along the coastline of the Kyushu island (top right), and vertical cross-section along the line of R-R′ in the direction of Philippine plate subduction (bottom right) [modified after *Tahara et al.*, 2008]. The land region is shown by gray, bold line in the figures on the right. Based on these and other cross-sections, regions with high Poisson's ratio (≥0.3 – yellow and red colors) were interpreted by *Tahara et al.* [2008] as quasi-elliptical, serpentinized domains similar to regions A and B in Figure 3b. Intersection of lines R-R′ and B-B′ is on the Miyazaki Plain. Red triangles show the active volcanoes. Circles indicate inter-plate earthquakes (see details in *Tahara et al.* [2008]). Gray vertical arrows indicate the aseismic crustal uplift. (b) Vertical cross-sections (left) located approximately along the line of R-R′ (top left) in Figure 3a and along a parallel line displaced ≈20 km north (bottom left) [modified after *Saiga et al.*, 2010]. Horizontal cross-section (right) is located at the depth of 30 km [also after *Saiga et al.*, 2010]. Colors represent the ratio of P- and S-wave velocities, V_p/V_s, which is related to the Poisson's ratio [e.g., *Mavko et al.*, 2003]. Gray rectangle above the vertical cross-section panel shows Kyushu Mountains. Ellipses represent regions with low velocity and low/moderate (black dashed line A) or high (black dashed line B) V_p/V_s ratio (see details in *Saiga et al.* [2010]). White circles indicate earthquake locations in the Philippine Sea Plate that converges under the Eurasia Plate.

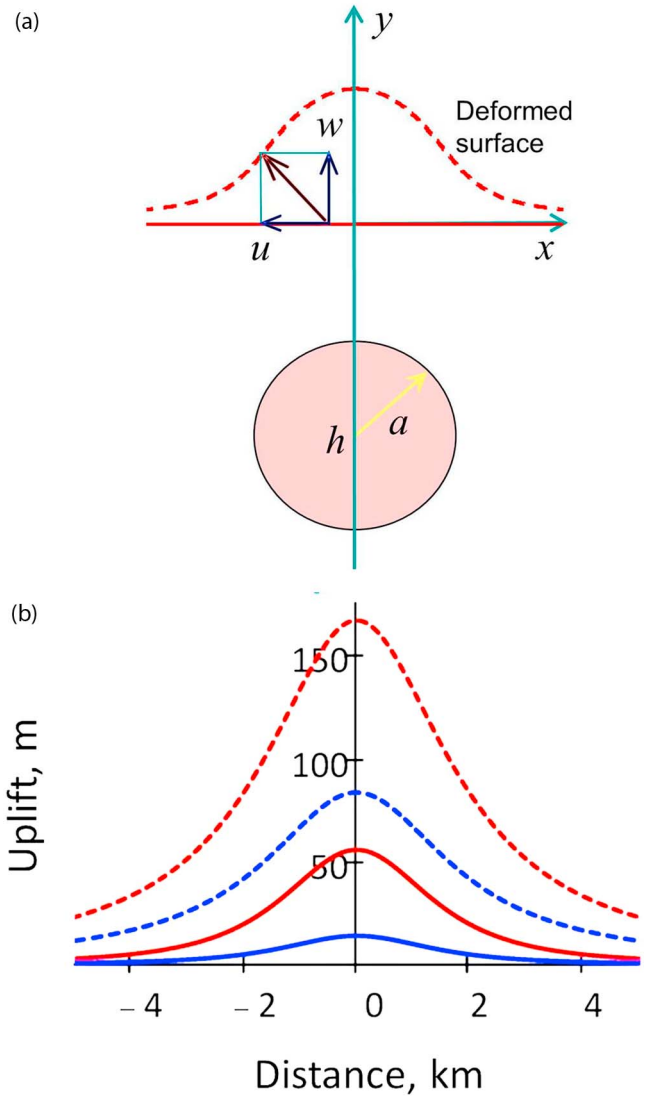

Figure 4. (a) A model of surface doming caused by subsurface serpentinization. Dashed line indicates the deformed surface over the center of the cylinder in the 2-D case and sphere in 3-D (with horizontal coordinate x replaced by the radial coordinate r). (b) Distribution of uplift, w, for spherical (solid lines) and cylindrical (dashed lines) inclusions of the same radius a = 1 km located at the depth of 2 km (red lines) and 4 km (blue lines). The uplift is given in meters (vertical axes) for ε_0 = 40% and the lateral coordinates r or x (horizontal axes) in kilometers.

as an isolated process. We apply these results to the TAG hydrothermal field and the Miyazaki Plain in Southwestern Japan and discuss possible connections between serpentinization and fault slip. A detailed analysis of the connection between serpentinization, microseismicity, and faulting in a region of large serpentinization strain that may be associated with the observed topographic salient at TAG is beyond the scope of this paper. We show, however, that serpentinization beneath the footwall of the detachment fault at TAG may enhance fault slip on the overlying normal faults. For the smaller strains that explain the uplift of the Miyazaki Plain, we show that serpentinization will tend to promote thrust-type events in some parts of the slip zone located near the upper boundary of the subducting Philippine Sea Plate underneath the Miyazaki Plain. Finally, we show that the rate of serpentinization needed to account for the uplift at TAG is likely too small to drive hydrothermal flow. The rate of serpentinization needed to produce the observed uplift at the Miyazaki Plain is significantly greater than that needed at TAG, though significantly smaller on per unit volume basis. As a result, the effects of serpentinization on the thermal regime in forearc wedge beneath the Miyazaki Plain may be small.

2. Scaling of Seafloor Uplift

[12] To incorporate two- or three-dimensional effects, we consider strain resulting from large-scale serpentinization based on the problem for an inclusion in the elastic half-space. The inclusion experiences homogeneous transformation strain (similar to homogeneous heating), ε_0, which is the homogeneous volumetric strain when the inclusion is allowed to expand freely. The physical nature of the transformation strain is attributed to the volumetric expansion resulting from the serpentinization reactions. Consider, for example, an inclusion of a given shape and volume V with a point, designated as the inclusion center, at the depth of h (Figure 4a). As a result of homogeneous serpentinization, the inclusion volume increases while its shape does not change. In a linearly elastic body, all displacements and stresses are proportional to the "loading" parameter, ε_0. In particular, the greatest vertical displacement on the seafloor, w_0, is also proportional to ε_0. Because the inclusion shape does not change, it can be characterized geometrically by its volume, V, in the 3-D case, and by its vertical cross-sectional area, S, in the 2-D case. Then, dimensional analysis suggests that w_0 is independent of the rock Young's modulus, E, and that in the 3-D case,

$$w_0 = \varepsilon_0 \frac{V}{h^2} f(\nu) \tag{1}$$

where $f(\nu)$ is the dimensionless function of the Poisson's ratio, ν. Table 1 lists symbols used and parameter values. Because the displacement of the half-space surface is given by that of the same plane within a full space, increased by a factor of $4(1-\nu)$ [*Mindlin and Cheng*, 1950; *Davies*, 2003], $f(\nu)$ in (1) is proportional to $1+\nu$, which also follows directly from the well-known results for the case of arbitrary 3-D distribution of mismatch strain in an infinite medium [*Goodier*, 1937; *Timoshenko and Goodier*, 1970].

[13] Similarly, dimensional analysis suggests that in the 2-D case,

$$w_0 = \varepsilon_0 \frac{S}{h} g(\nu) \tag{2}$$

where $g(\nu)$ is a dimensionless function of Poisson's ratio, ν, and, again, w_0 is independent of the rock Young's modulus, E. Note that hereafter, we use the same parameter of *volumetric* transformation strain, ε_0, for both 2-D and 3-D cases. This strain characterizes *free* 3-D expansion of an unconstrained body and is frequently measured in laboratory experiments. In this work, however, we assume plain strain conditions in the 2-D case, when "free" expansion is constrained in one direction and the volumetric strain is $(2/3)(1+\nu)\varepsilon_0$. Since the

Table 1. List of Symbols

Symbol	Definition	Value
	Latin Symbols	
a	major semi-axis of an elliptical inclusion	
a	radius of a cylindrical or spherical inclusion	
a_1, a_2	major semi-axes of inclined and sub-horizontal inclusions, respectively (Figure 9)	20, 30 km
a_1, a_2, …	complex coefficients in equation (B5)	
A	mean stress in the elliptic inclusion in an infinite plane (equation (9))	
b	minor semi-axis of an elliptical inclusion	
b_1, b_2	minor semi-axes of inclined and sub-horizontal inclusions, respectively (Figure 9)	7.5, 5 km
B	Skempton coefficient	0 - 1
c_1, c_2, …	complex coefficients in equation (B3)	
c_f	specific heat of fluid at high temperature	5×10^3 J/kg°C
c_r	specific heat of rock	10^3 J/kg°C
d	thickness of serpentinized layer in *Palmer*'s [1996] 1-D model	~1 km
$D(z)$	auxiliary function (equation (8))	
E	Young's modulus	10^{10} Pa
$f(\nu)$, $g(\nu)$	dimensionless functions of Poisson's ratio in equations (1) and (2)	
h	depth of the inclusion center	
L	inclusion size in horizontal direction (perpendicular to the plain of drawing in Figure 9)	~100 km
$\dot{M} = dM/dt$	serpentinization reaction rate	
$P(z)$	polynomial defined by asymptotic behavior of $D(z)$ at infinity	
Q	mass flow of hydrothermal fluid	
Q_s	mass flow of fluid absorbed in serpentinization reactions	$\sim 0.1\dot{M}$
r	radial coordinate	
R_1	$[\xi^2 + (\eta + \eta_0)^2]^{1/2}$ (Appendix A)	
R_2	$[\xi^2 + (\eta - \eta_0)^2]^{1/2}$ (Appendix A)	
S	cross-sectional area of a 2-D inclusion	
t	time	
u	horizontal or radial displacement	
V	inclusion volume	
V_p/V_s	ratio of P- to S-wave velocities	
w	vertical displacement	
w_P	vertical displacement of the seafloor in *Palmer*'s [1996] 1-D model	~100 m
w_0	largest vertical displacement of the seafloor	
x, y	horizontal and vertical coordinates	
X, Y	rotated coordinate set with X-axis aligned along the long axis of the inclusion and parallel to the fault plane or slip zone	
$z = x + iy$	complex coordinate	
z_0	complex coordinate of the inclusion center (Appendix B)	
	Greek Symbols	
α	coefficient of linear thermal expansion of rock	10^{-5}/°C
β	angle between the major axis of the inclusion and x-axis	
γ	latent heat released during serpentinization	4×10^5 J/kg
$\delta_1 = \varepsilon_0(1 + \nu)/3$	linear transformation strain in plain-strain conditions	
ΔI_1	change of the first stress invariant $\sigma_{xx} + \sigma_{yy} + \sigma_{zz}$ (or $\Delta\sigma_{xx} + \Delta\sigma_{yy} + \Delta\sigma_{zz}$)	
$\Delta p = -B\Delta I_1/3$	pore pressure change due to the Skempton effect	
ΔT	Coulomb stress on the fault plane or slip zone	
ΔT_s	temperature change resulting from serpentinization	
$\Delta\varepsilon_0$	incremental transformation strain	
$\Delta\sigma_{YY}$	normal stress change on the fault or slip zone plane	
$\Delta\tau_{XY}$	shear stress change on the fault or slip zone plane	
ε	small parameter $(a^2 - b^2)^{1/2}/h$	
ε_0	unconstrained, volumetric transformation strain	
ϕ	serpentinized fraction of the inclusion volume	
$\zeta = \xi + i\eta$	complex coordinate on the infinite plane	
$\eta = y/a$	normalized vertical coordinate (Appendix A)	
$\eta_0 = h/a$	dimensionless depth of the inclusion (Appendix A)	
θ	fault angle in counter-clock direction with respect to the horizontal	
$\kappa = 3 - 4\nu$	plain-strain modulus	
λ	complex coefficients (equation (B3))	
μ	shear modulus	
ν	Poisson's ratio	0.25
$\xi = x/a$	normalized horizontal coordinate (Appendix A)	
$\rho = x/h$, r/h	dimensionless lateral or radial coordinate (Section 2)	

Table 1. (continued)

Symbol	Definition	Value
ρ_r	density of serpentine	≈2500 kg/m^3
σ_{xx}, σ_{yy}, σ_{zz}, τ_{xy}	stress components in (x, y) coordinate set	
τ_0	background (initial) tectonic shear stress on the fault or slip zone plane	
$\varphi(z)$, $\psi(z)$	*Muskhelishvili*'s [1979] stress functions	
$\omega(\zeta)$	conformal mapping of inclusion exterior onto the exterior of the unit circle in the infinite plane	
$\omega^{-1}(z)$	inverse function of $\omega(\zeta)$	

results are often expressed through the plain-strain, 'free' linear expansion strain $\delta_1 = (1/3)(1 + \nu)\varepsilon_0$ [e.g., *Ru*, 1999; *Aderogba and Berry*, 1971], it is worth mentioning that in (2) and below, we use the same volumetric, transformation strain, ε_0, as in (1). In this formulation, 2-D and 3-D cases do not differ and, therefore, $g(\nu)$ in (2) is also proportional to $1 + \nu$. Using δ_1 instead of ε_0 in (1) and (2) would eliminate their dependence on ν, and, therefore, w_0 would be independent of material properties.

[14] As a particular case, consider a spherical inclusion of radius a, with its center at depth h, in the half-space $y < 0$ as shown in Figure 4a. We use the cylindrical coordinate system (r, y), with horizontal coordinate r replacing the radial coordinate x, and the surface $y = 0$ represents the seafloor. Assuming that the inclusion lies entirely below the half-space surface ($h \geq a$), vertical and radial displacements of the seafloor, can be calculated as [*Mindlin and Cheng*, 1950; *Nowacki*, 1986]

$$w = \frac{w_0}{(1+\rho^2)^{3/2}}, \quad u = \frac{w_0 \rho}{(1+\rho^2)^{3/2}} \tag{3}$$

respectively, where $w_0 = (1 + \nu)V\varepsilon_0/(3\pi h^2)$, $\rho = r/h$ is the normalized radial coordinate, and the inclusion volume $V = (4/3)\pi a^3$. In this case, therefore, $f(\nu) = (1 + \nu)/(3\pi)$.

[15] Figure 4a shows schematically the surface deformation resulting from serpentinization of a spherical volume. Equation (3) suggests that, depending on parameters h (a few km) and V ($\sim$ 1–10 km^3), maximum surface uplifts range between a few tens and a few hundreds of meters for $\varepsilon_0 \sim 0.1 - 0.5$. Such projected uplifts are similar to those estimated by *Palmer* [1996] using a 1-D model. In his model, the vertical displacement of the seafloor is uniform and, if the lateral strain is negligible, equals to $w_P = (1 + \nu)\varepsilon_0 d/[3(1 - \nu)]$, where d is the thickness of the serpentinized layer (Figure 1b). For $d \sim 1$ km and $\varepsilon_0 \approx 50\%$, $w_P \sim 100$ m. The horizontal extent of the uplifted area and uplift distribution cannot be estimated from *Palmer*'s [1996] model, however. As discussed below, these are naturally included in the 2- and 3-D models of serpentinized inclusion. In addition, w_P is independent of the depth of the serpentinized layer, whereas the uplift caused by a finite domain decreases with the depth according to equations (1) and (2).

[16] In the model of spherical inclusion, w_0 depends upon both the inclusion radius and depth, but the shape of the uplift in (3) is independent of the radius. According to equation (1), the horizontal extent of the uplifted region (Figure 4a) can be defined as $\rho = 1$, where the vertical displacement becomes $2^{-3/2}w_0 \approx w_0/2.8$. In other words, the uplift "width" scales with the inclusion depth, but is independent of its size (volume).

[17] Let us now consider a cylindrical inclusion of radius a, with the center at a depth of h in a rectangular coordinate system (x, y), with horizontal coordinate x replacing the radial coordinate r in Figure 4a. In this case, the distribution of surface displacements is given by expressions

$$w = \frac{w_0}{1+\rho^2}, u = \frac{w_0 \rho}{1+\rho^2} \tag{4}$$

similar to equation (3) and obtained by integrating the solution of *Mindlin and Cheng* [1950] for a dilation center in a half-space (see also Appendix A). Here $w_0 = 2(1 + \nu)S\varepsilon_0/(3\pi h)$, $\rho = x/h$ is the dimensionless lateral coordinate, and the cross-sectional area of the inclusion $S = \pi a^2$. Hence, $g(\nu) = 2(1 + \nu)/(3\pi)$ in equation (2). As in the case of the spherical inclusion, the maximum of the surface uplift depends on both inclusion size and depth, whereas the shape of the surface uplift is independent of size but scales with the inclusion depth.

[18] The largest vertical displacement on the seafloor for a spherical inclusion is $[(1 + \nu)(2/9)(a/h)]^{-1}$ times smaller than for a cylindrical one of the same radius. To place this in context, we plotted the uplift distributions given by equations (3) and (4) in Figure 4b. As expected, serpentinization in an extended cylindrical region would result in larger surface displacement than that resulting from a more compact spherical region.

3. An Elliptical Inclusion

[19] Although the simple scaling considered above provides some insight into understanding-multidimensional uplift process caused by the subsurface serpentinization, to address the effect of the inclusion shape, one needs solutions for displacements and stresses inside and outside of the inclusion of various shapes. In order to perform a parametric analysis, it is preferable to have closed form solutions. For this purpose, we consider here a half-space containing an inclusion of elliptical shape. This solution is sufficiently general for a wide variety of settings, and it reduces to the simple cylindrical solution above. We will then discuss applications of these solutions to the TAG region on the Mid-Atlantic Ridge (Figure 2) and the Kyushu region above the subducting Philippine Sea plate (Figure 3).

[20] To perform the stress-strain analysis for an elliptical inclusion in a half-space, we employ the complex variable technique. The elastic field can be represented by the well-known expressions [*Muskhelishvili*, 1979]

$$\begin{cases} \sigma_{xx} + \sigma_{yy} = 2[\varphi'(z) + \overline{\varphi'(z)}] \\ \sigma_{yy} - \sigma_{xx} + 2i\tau_{xy} = 2[\bar{z}\varphi''(z) + \psi'(z)] \\ 2\mu(u + iw) = \kappa\varphi(z) - z\overline{\varphi'(z)} - \overline{\psi(z)} \end{cases} \tag{5}$$

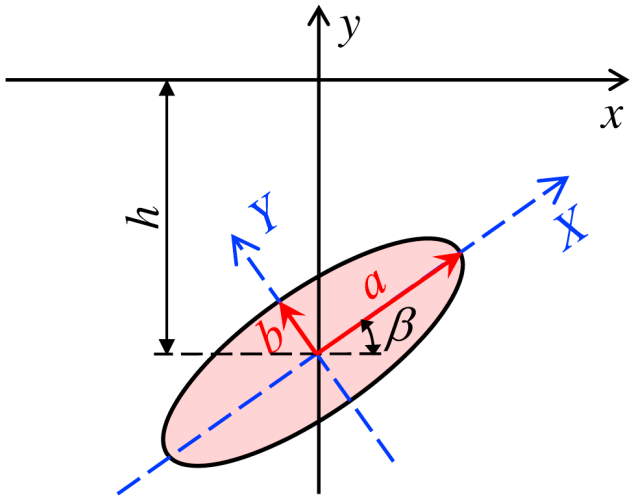

Figure 5. A model of elliptical domain of subsurface serpentinization. The domain is located in the half-space $y \le 0$, $-\infty < x < \infty$ and the major ellipse axis is aligned with coordinate axis, X, in rotated coordinate set X, Y.

where σ_{xx}, σ_{yy}, and τ_{xy} are the stress components in (x, y) coordinate set (Figure 5), u and w, are the vertical and horizontal displacements in the half-space, $z = x + iy$, bars represent complex conjugates, $\kappa = 3 - 4\nu$ in plain strain conditions, $\mu = E/[2(1 + \nu)$ is the shear modulus, ν is the Poisson's ratio, and $\varphi(z)$ and $\psi(z)$ are the *Muskhelishvili*'s [1979] stress functions. For an inclusion of arbitrary shape undergoing homogeneous transformation strain, ε_0, in an elastic half-space, these functions can be written as [*Ru*, 1999; *Ru et al.*, 2001]

$$\varphi(z) = A[\overline{D(\bar{z})} - \overline{P(\bar{z})} - z/2], \quad \psi(z) = -A[z\overline{D'(\bar{z})} - z\overline{P'(\bar{z})} - P(z)] \tag{6}$$

inside the inclusion, and

$$\varphi(z) = A[\overline{D(\bar{z})} - \overline{P(\bar{z})}], \quad \psi(z) = -A[z\overline{D'(\bar{z})} - z\overline{P'(\bar{z})} + D(z) - P(z)] \tag{7}$$

outside. Here

$$D(z) = \overline{\omega[1/\overline{\omega^{-1}(z)}]} \tag{8}$$

and coefficient

$$A = (4/3)\mu(1 + \nu)\varepsilon_0/(\kappa + 1) \tag{9}$$

is equal to the absolute value of the mean homogeneous stress, $(\sigma_{xx} + \sigma_{yy})/2$, caused by the same transformation strain, ε_0, inside the same inclusion if it were located in the infinite plane. This can be shown by using the corresponding solution for the 2-D Eshelby inclusion [e.g., *Jaswon and Bhargava*, 1961] or directly from equations (5), (6), (7), and (11) as the inclusion depth $h \to \infty$.

[21] In equations (6)–(8), $z = \omega(\zeta)$ is conformal mapping of the region outside the inclusion in the infinite complex plane $z = x + iy$ onto the exterior of the unit circle, $|\zeta| = 1$, on the infinite complex plane $\zeta = \xi + i\eta$, $\omega^{-1}(z)$ is the inverse function of $\omega(\zeta)$, and $P(z)$ is the polynomial of finite degree defined from the asymptotic behavior $D(z) = P(z) + o(1)$ $(z \to \infty)$ of $D(z)$ at infinity. This means that $\omega(\zeta)$ cannot be arbitrary but should result in function $D(z)$, defined by equation (8), with such a property. Specifically, function $D(z)$ should be analytic everywhere in the exterior of the inclusion except, perhaps, at infinity where it has a pole of finite degree [*Ru*, 1999]. Such functions $\omega(\zeta)$ describe a rather broad class of domains, which includes inclusions of elliptical or more general shapes (see Appendix B).

[22] Because $P(z)$ is obtained directly from $D(z)$, the advantage of *Ru*'s [1999] representation (6)–(8) is that two unknown functions, $\varphi(z)$ and $\psi(z)$, are expressed through one auxiliary function $D(z)$. In addition, the same mapping $\omega(\zeta)$ is used for the problem of an inclusion in the infinite plane and in the semi-plane. Choosing function $D(z)$ in the form of (8) guarantees that stress functions (6), (7) result in continuous tractions and displacements on the interface between the inclusion and host medium. These functions also satisfy the boundary conditions of zero tractions on the free half-space boundary [*Ru*, 1999].

[23] Inclusion shape and functions $D(z)$ and $P(z)$ are fully defined by the conformal mapping $\omega(\zeta)$. Once functions $D(z)$ and $P(z)$ are found, the stress state and displacements are computed using equation (5). Using mapping $\omega(\zeta) = [(a + b)\ \zeta + (a - b)\ \zeta^{-1}]2^{-1} - hi$, *Ru* [1999] obtained these functions for an elliptical inclusion with one axis parallel to the half-space boundary and its center located at depth h on the coordinate axis (i.e., when $\beta = 0$ in Figure 5). If the inclusion is inclined (Figure 5) and the angle between the inclusion and x-axis is β, the function $\omega(\zeta)$ and its inverse $\omega^{-1}(z)$ can be written as (Appendix B)

$$\omega(z) = -ih + \frac{e^{i\beta}}{2}\left[(a+b)\zeta + \frac{a-b}{\zeta}\right],$$
$$\omega^{-1}(z) = \frac{e^{-i\beta}(z+ih)}{a+b}\left[1 + \sqrt{1 - \frac{e^{2i\beta}(a^2-b^2)}{(z+ih)^2}}\right] \tag{10}$$

Hereafter, a and b are the major and minor ellipse semi-axes, respectively. In the case of (10) (Appendix B),

$$D(z) = ih + \frac{(a+b)e^{-i\beta}}{2\omega^{-1}(z)} + \frac{e^{-i\beta}(a-b)}{2}\omega^{-1}(z),$$
$$P(z) = ih + \frac{a-b}{a+b}e^{-2i\beta}(z+ih) \tag{11}$$

Since functions $D(z)$, $P(z)$ are known from expressions in (11), stresses and displacements everywhere in the half-space and inclusion can now be computed using equations (5), (6), and (7). Taking into account that $z = \bar{z} = x$ on the surface $y = 0$ of the half-space $y < 0$, we obtain (Appendix B) the serpentinization-induced displacements

$$u(x,0) + iw(x,0) = \frac{4ab\varepsilon_0}{3(a^2-b^2)}(1+\nu)e^{2i\beta}(x - ih)[1 - U(x)] \tag{12}$$

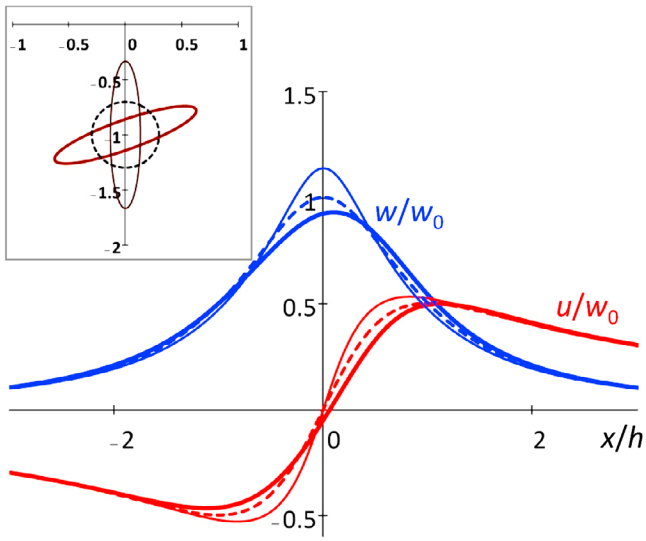

Figure 6. Normalized vertical (w/w_0, blue lines) and horizontal (u/w_0, red lines) surface displacements over serpentinized regions (inclusions) as functions of normalized horizontal coordinate (x/h). Thin and bold solid lines correspond to the vertical ($\beta = 90°$) and inclined ($\beta = 20°$) elliptic ($a/b = 5$) inclusions, respectively. Dashed lines correspond to the circular ($a/b = 1$) inclusion. The inclusions are shown in the insets in normalized coordinates (x/h, y/h), located at the same depth ($h/a = 1.5$), and have the same cross-sectional area ($S/h^2 = 4\pi/45 \approx 0.279$).

and stresses

$$\sigma_{xx}(x) = -\frac{16\mu\varepsilon_0}{\kappa+1}\, ab\, \frac{1+\nu}{3} \cdot \left[\frac{1}{(x+ih)^2(1+\overline{U(x)})\overline{U(x)}} + \frac{1}{(x-ih)^2(1+U(x))U(x)}\right] \quad (13)$$

on the seafloor. Here

$$U(x) = \sqrt{1 - \frac{e^{-2i\beta}(a^2-b^2)}{(x-ih)^2}} \quad (14)$$

Stresses $\sigma_{yy} = \tau_{xy} = 0$ are the boundary conditions on the half plane boundary. Note that the quantity in brackets in (13) is real because it is the sum of two conjugate complex numbers.

[24] When $a^2 - b^2 \ll h^2$, the fraction term under the square root in equation (14) is small, and (12) reduces to equation (4) for a cylindrical inclusion, except now $S = \pi ab$ is the cross-sectional area of the elliptical inclusion. This shows that when $b \to a$, equation (4) is recovered from equations (12) and (14) as a particular case. This also shows that for a deep inclusion ($h \to \infty$ or $h \gg a$), the uplift is independent of the inclusion orientation and aspect ratio, but is only affected by its volume (or area), where material is transformed by serpentinization. Furthermore, because the *Mindlin and Cheng*'s [1950] solution for the dilation center in a half-space can be used as a Green's function, such a deep inclusion does not need to be elliptical, but can be of *arbitrary* shape that has cross-sectional area S, and equation (4) are still applicable to describe the surface deformation. Likewise, stress σ_{xx} at the seafloor in (13) is also independent of inclusion shape for a sufficiently deep inclusion. In this case, σ_{xx} is the same as that for a circular inclusion of the same cross-sectional area S or for the corresponding point (linear) source of dilation.

4. Uplift Resulting From Subsurface Serpentinization

4.1. Effects of Depth and Shape of Serpentinized Domain

[25] To understand possible effects of subsurface serpentinization on the seafloor uplift, we plotted the distribution of the surface displacements when the serpentinized domain with aspect ratio $a/b = 5$ is located at the depth of $h/a = 1.5$ and inclined at the angle of $\beta = 20°$ to the horizontal (solid bold lines in Figure 6). For comparison, we also plotted the seafloor displacements that would be caused by a circular region of the same area S as an ellipse and located at the same depth h (dashed lines in Figure 6). Hereafter in this section, displacements are normalized by the maximum vertical uplift $w_0 = 2(1+\nu)S\varepsilon_0/(3\pi h)$ that would be caused by the circular domain (or dilational source) while coordinates are normalized by the inclusion depth.

[26] Because the elliptical domain is inclined in this example, the vertical uplift (bold blue, solid line in Figure 6) is asymmetric. Neither vertical nor horizontal displacements, however, differ significantly for the cases of elliptical and circular inclusions. This means that the asymptotic approximation of large depth ($h \gg a$) is applicable even for a relatively shallow inclusion ($h/a = 1.5$ in Figure 6). Because the asymptotic solutions corresponding to large depth do not include the inclusion angle (equation (4)), however, this also means that the uplift is relatively insensitive to the angle. In the case of a vertical inclusion of the same aspect ratio ($a/b = 5$) and depth (thin solid lines in Figure 6), the distance, $h - a$, between the upper end of the vertical inclusion and the seafloor is only 25% of the inclusion size, $2a$. Even in this relatively extreme case, the uplift generated by the vertical inclusion differs from that resulting from a circular inclusion of the same volume by no more than by 20%; and even this difference is only noticeable directly above the top of the inclusion (Figure 6).

[27] Figure 7a shows vertical displacements generated by inclusions with $h/a = 1.8$. The uplifts caused by the inclusions of three different inclinations (0, 45°, and 90°) do not differ from the case of equivalent circular domain by more than 7%. This does not mean that the difference cannot be more significant, however. An example for $a/b = 10$, $h/a = 0.4$, and $\beta = 10°$ is shown in Figure 7b. In this case, the approximation by an equal-area inclusion (shown on the inset) may not be sufficiently accurate as the difference compared to the exact solution (ellipse on the inset in Figure 7b) can be nearly 100%. In general, from a practical standpoint, the uplift caused by an elliptical inclusion deviates from a circular inclusion when $h/(2a) < 0.75$, and the difference becomes more significant (50% or more) when $h/(2a)$ is less than 0.5.

4.2. Application to TAG

[28] Figure 2 shows the central portion of the east wall of the axial valley at the TAG hydrothermal field (Mid-Atlantic

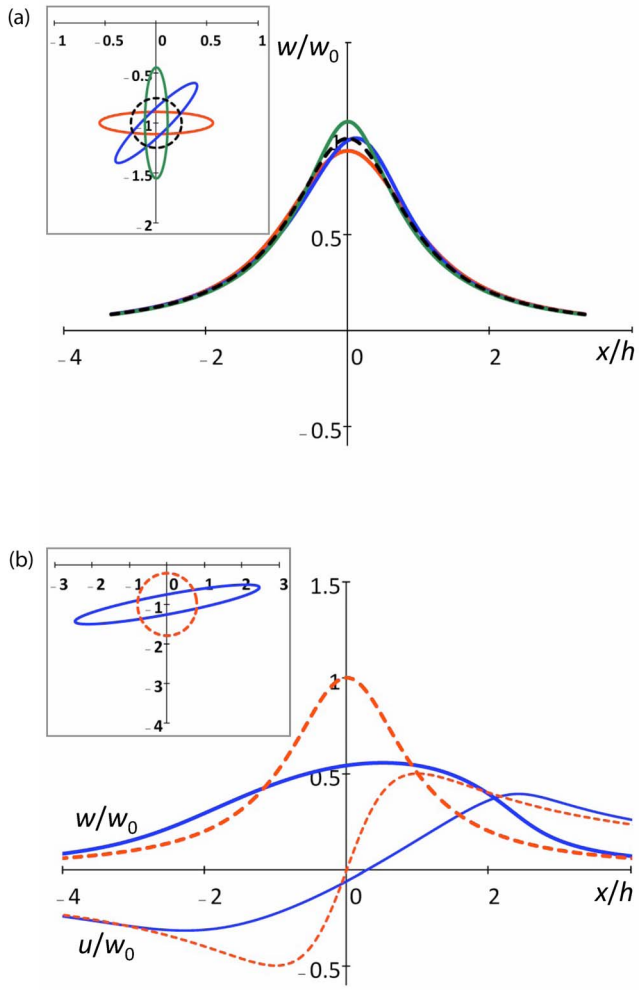

Figure 7. Normalized surface displacements caused by sub-surface serpentinization in different domains (shown in the insets in normalized coordinates x/h and y/h) as functions of normalized horizontal coordinate (x/h). (a) Normalized uplifts, w/w_0, caused by elliptical (a/b = 5) inclusions of different inclinations (horizontal – red line, vertical – green line, and inclined at 45° – blue line) and circular inclusion (dashed line) of the same cross-sectional area ($S/h^2 = 4\pi/45 \approx 0.279$) and depth ($h/a$ = 1.8). (b) Normalized vertical (w/w_0, bold lines) and horizontal (u/w_0, thin lines) surface displacements over inclined elliptical (β = 10°, a/b = 10, solid lines) and circular (a/b = 1, dashed lines) inclusions that are located at the same depth (h/a = 0.4) and have the same cross-sectional area ($S/h^2 = 5\pi/8 \approx 1.963$).

Ridge). The rounded area centered near 26°08.7′N, 44°49.6′W exhibits an anomalous salient that projects about 3.5 km westward into the axial valley. The salient encompasses a domed area about 3 km in diameter (Figure 2) bounded by the 3725 m and 3625 m isobaths thus indicating a relief of about 100 m. We hypothesize that the observed salient may be a result of serpentinization of a crustal region and determine the volume and the depth of this region that would be consistent with the observed uplift (Figure 2).

[29] We use equation (3) for a sub-surface spherical inclusion to model the TAG salient (Figure 2). As in 2-D case, it can be shown that uplift resulting from a deep 3-D inclusion ($h \gg a$) is independent of the inclusion shape and is only affected by its volume. In other words, such a deep inclusion need not be spherical, but can be of *arbitrary* shape with the same volume V, and equation (3) still adequately describe the surface deformation. Furthermore, as shown in the previous section, the asymptotic approximation of large depth ($h \gg a$) is applicable in 2-D even for h/a = 1.5 (or $h/(2a)$ = 0.75). Because the interaction between the inclusion and the surface is weaker in 3-D than in 2-D, the solution (3) for large depth is applicable even for shallower inclusions.

[30] According to equation (3), the horizontal extent of the uplifted region scales with the inclusion depth. Hence, the 3.5-km-wide TAG salient could have resulted from serpentinization in a region centered at a depth of 1.5 to 2.5 km. The red dashed lines in Figure 8 show the distribution of vertical uplift resulting from partial serpentinization, ε_0 = 20%, in a volume V = 25 km^3 centered at a depth of h = 2.5 km. The radius of a spherical inclusion corresponding to this volume would be a = 1.8 km (red dashed line in the inset in Figure 8a), but the inclusion does not need to be spherical because in this case h/a = 1.4, and the asymptotic expression (3) is sufficiently accurate (and, in-fact, more accurate than in 2-D case). The blue solid lines in Figure 8 show uplift resulting from more complete serpentinization, ε_0 = 40%, in a smaller volume, V = 5 km^3, centered at a depth of h = 1.6 km. The corresponding equivalent spherical domain has a radius a = 1.1 km, and the ratio h/a = 1.5 indicates again that, within limits, the domain can be of arbitrary shape.

[31] For example, suppose that a 3-D elliptically shaped inclusion, considered in 2-D in Section 4.1 (a/b = 5, h/a = 1.5, β = 20°) (Figure 5), is located on the footwall side of the TAG detachment fault (Section 2), where gabbro outcrop (Figure 2a) [*Zonenshain et al.*, 1989] and seismic data suggests the presence of lower crustal and/or serpentinized upper mantle rocks at anomalously shallow depths [*deMartin et al.*, 2007; *Canales et al.*, 2007]. In this case, the inclusion dimensions could be $2a$ = 4 km and $2b$ = 0.8 km ($V = \pi a^2 b$ = 5 km^3). If the inclusion center were located at the depth of h = 1.6 km, the salient topography would again be given by the blue solid lines in Figure 8 and would be reasonably close to the observed topography (Figure 2).

[32] Based on structural observations and seismic and magnetic data, a detachment fault is present in the wall of the axial valley along the eastern margin of the salient. The fault consists of roughly two segments. The shallow segment is inclined at ≈20° and the deep part of the fault has an angle of ≈70° [*deMartin et al.*, 2007]. The salient is underlain by the shallow part of the fault at a depth of ∼2 km. The detachment fault may be a conduit for the flow of water into the mantle rock where serpentinization occurs. Our model suggests that the observed salient may have been produced by serpentinization of upper mantle peridotite rocks that were displaced by faulting to a relatively shallow depth of ∼2 km. As Figure 7 indicates, serpentinization of 5 to 25 km^3 located beneath the footwall of the TAG detachment fault would be consistent with the existence of the salient on the seafloor.

[33] It is important to mention, however, that 20 to 40% of transformation strain would most likely be beyond the elastic limit of serpentinized rock [*Jaeger et al.*, 2007]. Hence, plots in Figure 8 probably correspond to the lower limit of the expected seafloor deformation. After serpentinization begins,

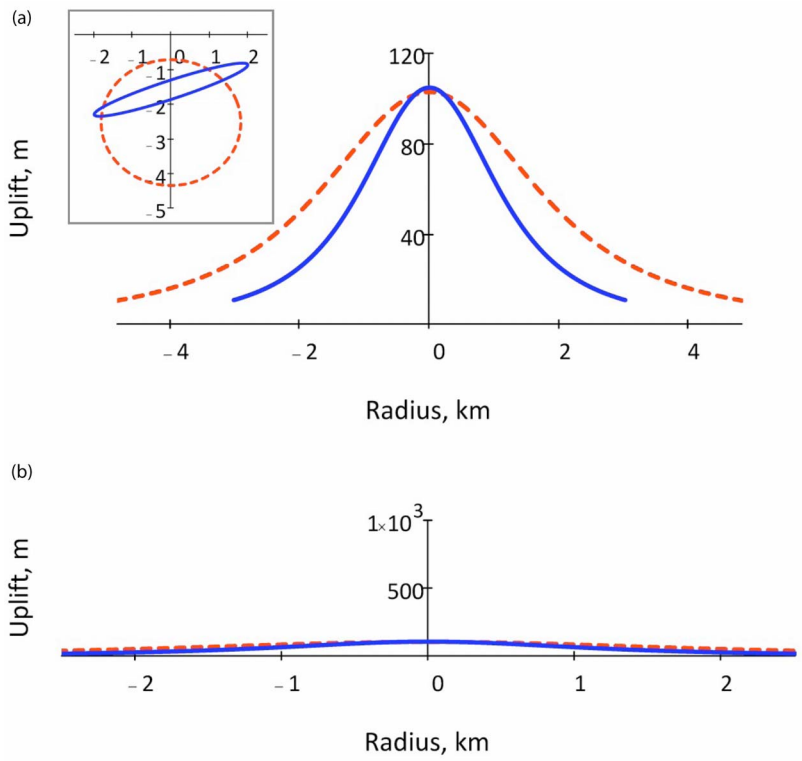

Figure 8. An elastic model of the TAG salient topography resulting from partial serpentinization (ε_0 = 20%) of 25 km^3 of rock at the depth of 2.5 km (red dashed line) and massive serpentinization (ε_0 = 40%) of 5 km^3 at the depth of 1.6 km (blue solid line). (a) Uplift scale (vertical axis) is increased for better visualization. The corresponding geometries and depths of possible serpentinized bodies are shown on the inset. The elliptical inclusion is inclined to the horizontal at the angle of $\beta = 20°$. (b) Same as Figure 8a but vertical and horizontal scales are equal.

multiple faulting and fracturing events would probably occur at a transformation strain of several percent (or less), which is much lower than the 40% volume expansion corresponding to massive serpentinization. Such events may occur both inside and outside the serpentinized region and thus may contribute to the development of the detachment fault, rock permeability, and water flow required for serpentinization (Section 6.3).

[34] The age of TAG mound $\sim 10^5$ years is nearly the same as the lithospheric age [*Lalou et al.*, 1995]. Therefore, the transformation strain of 20 to 40% can be interpreted as total strain rather than the strain increment. In the next section, we consider an example of transformation strain corresponding to the serpentinization increment that may be small compared to the overall serpentinization level.

4.3. Application to the Kyushu-Palau Subduction Zone

[35] *Tahara et al.* [2008] attribute the observed Quaternary uplift of the Miyazaki Plain (Figure 3) to the subduction of the Kyushu-Palau Ridge. They hypothesize that the Ridge might have been detached from the subducted slab below 30 km depth by some mechanism. They further conjecture that the subducting slab may steeply bend due to a loss of buoyancy beneath the Kyushu Island [*Tahara et al.*, 2008, Figures 2 and 8] causing the detached Kyushu-Palau Ridge to move upwards [*Tahara et al.*, 2008, Figure 14b]. Based on this argument, *Tahara et al.* [2008] suggest that relatively low density materials of the Kyushu-Palau Ridge might have caused the significant aseismic crustal uplift of ~120 m during the past ~120 thousand years at the Miyazaki Plain.

[36] While buoyancy may indeed be an important factor for the crustal uplift observed on the Miyazaki Plain, an alternative and somewhat simpler mechanism could be the volume expansion in the serpentinized regions identified by seismic studies [see *Tahara et al.*, 2008, and references therein]. In this scenario, the crustal uplift may have resulted from the serpentinization of mantle rock in the inclined region beneath the Miyazaki Plain and, perhaps, in a sub-horizontal region located near the base of the crust west of the subducted Kyushu-Palau Ridge (see Figure 3).

[37] A serpentinized region in the mantle forearc beneath the Miyazaki Plain is consistent with seismic data [*Tahara et al.*, 2008; *Saiga et al.*, 2010] suggesting an elevated Poisson's ratio (Figure 3). Serpentinization likely occurs as water fluxed from the downgoing slab and sediments ascends to the forearc [e.g., *Hyndman et al.*, 1997]. Thermal modeling suggests that maximum temperatures are 350–400°C in the region beneath Hyuganada [*Hyndman et al.*, 1995], which is favorable for serpentinization. Hence, based on the seismic data presented by *Tahara et al.* [2008] and *Saiga et al.* [2010], a 2-D elliptical inclusion could be used to model this region (Figure 3).

[38] The nature of the sub-horizontal low-velocity, near-normal or low Poisson's ratio region A (Figure 3) is less

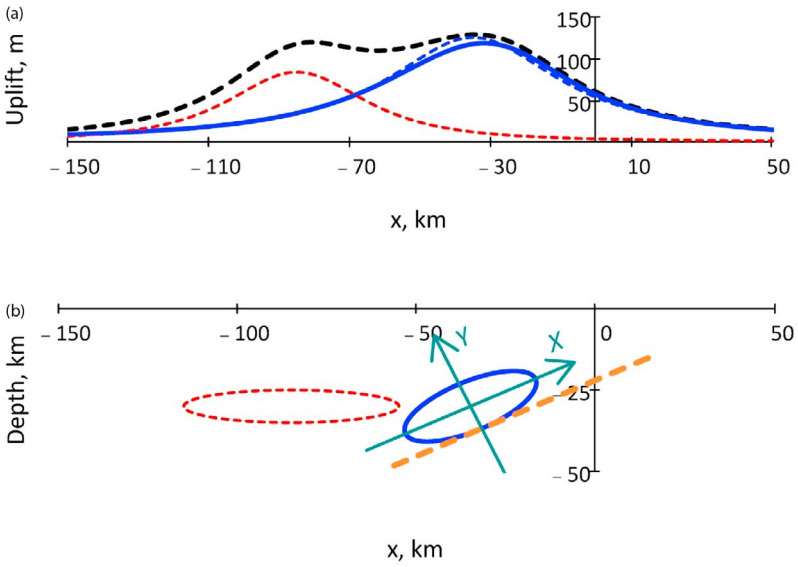

Figure 9. An elastic model of the uplift on Kyushu Island resulting from partial serpentinization ($\varepsilon_0 = 3\%$) of mantle and lower crust. (a) Individual uplifts caused by the sub-horizontal (red dashed line) and inclined (blue solid line) serpentinized regions (Figure 9b) and the resulting uplift (black dashed line) caused by these regions together. Blue dashed line indicates the vertical uplift caused by the cylindrical inclusion of the same cross-sectional area as the inclined elliptical inclusion. (b) A configuration of two inclusions representing serpentinized regions (with higher Poisson ratio inferred from the seismic tomography data) in Figure 3. The inclined ($\beta = 25°$) and sub-horizontal regions are modeled by a 2-D elliptic inclusion and a 3-D oblate spheroid, respectively, centers of which are located at the depth of $h = 30$ km. The inclusions have the thickness of $2b_1 = 15$ km and $2b_2 = 10$ km, respectively, and they have the lengths of $2a_1 = 40$ km and $2a_2 = 60$ km. They can be viewed as representing the sub-horizontal region A and inclined region B in Figure 3b. The coordinate set X, Y is shown by the thin green lines with X-axis along the major axis of the inclined inclusion and parallel to the upper boundary of the subducting plate (and slip zone). Bold orange dashed line indicates the aseismic slip zone shown in Figure 3a (bottom right) by blue line.

clear. *Saiga et al.* [2010] conclude that ratio V_p/V_s of P- and S-wave velocities is low in this region. They hypothesize the accretion of low-density rocks (of a detached Kyushu-Palau Ridge) at the bottom of the crust at the depth of ~30 km beneath the Kyushu Mountains [*Saiga et al.*, 2010, Figure 15]. *Tahara et al.* [2008] offer a similar explanation. Because the mechanisms of mantle hydration in the sub-horizontal region is not obvious [*Salah and Seno*, 2008], we consider below both possibilities of ongoing (but small) and absent serpentinization in this region. We represent the sub-horizontal ellipse shown in domain A in Figure 3b by a 3-D ellipsoidal inclusion (oblate spheroid).

[39] We assume the characteristic inclination $\beta \approx 25°$ of the inclined region and its characteristic size (in the vertical cross-section) of $2a_1 \sim 40$ km. The sub-horizontal region appears to be somewhat larger (Figure 3b), so we assume $2a_2 \sim 60$ km. We finally assume that both regions are located approximately at the same depth of $h \sim 30$ km and have the same cross-sectional area, which results in the thicknesses of $2b_1 \sim 15$ km and $2b_2 \sim 10$ km for the inclined and sub-horizontal inclusion, respectively (Figure 3b).

[40] Figure 9a shows the individual uplift distributions above the horizontal (red dashed line) and inclined ($\beta = 25°$, blue solid line) elliptical inclusions with such parameters (Figure 9b). From the solution discussed in Section 3, one can compute stresses and displacements not only for a single elliptic inclusion, but also for multiple inclusions in the half-space as long as inclusions do not overlap and do not intersect the half-space boundary. This superposition is also permissible for a combination of 2-D (inclined) and 3-D (sub-horizontal) inclusions (Figure 9b).

[41] The combined uplift caused by both inclusions (black dashed line in Figure 9a) is significantly more uniform than the uplifts that would have been caused by each inclusion separately (solid red and blue lines in Figure 9a). A transformation strain of $\varepsilon_0 = 3\%$, used for calculations shown in Figure 9, generates uplift close to the detected ~120 m of the Quaternary uplift of the Miyazaki Plain and the mountain range at central part of the Kyushu Island (west of the Miyazaki Plain in Figure 3). The horizontal extent of the uplifted region is $\sim 10^2$ km (Figure 9a), which is consistent with the scales of topographical features on the Kyushu Island. Because the inclined inclusion is sufficiently deep ($h/a_1 = 1.5$), the difference between the exact solution (blue solid line in Figure 9a) and that for the equivalent cylinder (blue dashed lines in Figure 9a) is negligible. For the 3-D sub-horizontal inclusion, $h/a_2 = 1$. Since the interaction between the inclusion and the surface is weaker in 3-D than in 2-D, we used the equivalent sphere (or point source) solution to plot the surface displacement caused by the sub-horizontal inclusion (red dashed line in Figure 9b). Because the surface displacements decay faster in 2-D than in 3-D with the increasing distance from the inclusion, the sub-horizontal inclusion does not significantly affect the surface

uplift of the Miyazaki Plain (i.e., above the inclined inclusion). In contrast, the 2-D-like inclined region contributes nearly 30% of the uplift of the Kyushu Mountains above the sub-horizontal low-velocity region. We are not aware of uplift data north of the Miyazaki Plain, but it would be informative to compare the prediction of our model to the actual uplift in the coastline area east of the Kyushu Mountains. Since the sub-horizontal inclusion would not significantly affect the uplift there, we expect uplift in the range of $\sim 10^2$ m.

[42] We note that the uplift associated with serpentinization occurs over ~120 ka whereas subduction has been occurring for more than 10 Ma [*Seno and Maruyama*, 1984]. Hence, the serpentinization process may be viewed as incremental. That is, $\varepsilon_0 = 3\%$ may be a $\Delta\varepsilon_0$ superimposed on previous serpentinization processes. The inferred larger value of Poisson's ratio in this region would not necessarily be inconsistent with a 6% increment in the amount of serpentinization occurring in the past 120 ka. On the other hand, in the region beneath Northern Kyushu, elevated Poisson's ratio above the subducting slab may be a result of fluid-filled cracks induced by the slab dehydration [*Salah and Seno*, 2008]. In this case, the total level of serpentinization may be small (e.g., several percent) and only slightly contribute to an elevated value of Poisson's ratio.

[43] Similarly, ratio V_p/V_s in the sub-horizontal, low-velocity region, identified by *Saiga et al.* [2010] beneath the Kyushu Mountains (Figure 3b), may be relatively low because the serpentinization in this region does not exceed a few percent. The aseismic uplift of the Kyushu Mountains appears to be ongoing over the last 2 Ma [*Kamata and Kodama*, 1999; *Saiga et al.*, 2010]. If during this time period, the uplift has been primarily caused by the serpentinization processes, the total level of serpnetinization in the low-velocity region A in Figure 3b is unlikely to exceed several percent in order to be consistent with the uplift of $\sim 10^2$ m. Our results, therefore, may help to constrain the level of serpentinization in this region.

[44] In general, the geological situation near Kyushu Island is quite complicated (e.g., Figure 3) and other mechanisms may be contributing to the ongoing crustal uplift. Yet our simple elastic model appears to adequately describe the uplift magnitude, and it is consistent with the geological structure inferred from the seismic data as well as with available data on the Quaternary crustal uplift determined from the shoreline heights [*Shimoyama et al.*, 1999; *Nakada et al.*, 2002]. The required serpentinization strain increment of 3% is much smaller than in the TAG salient case (Section 4.2), and could be more consistent with the assumption of linear elastic model.

5. Localized Failure Associated With Serpentinization

[45] In previous sections we focused primarily on the uplift associated with a serpentinized region at depth by calculating the elastic strains caused by subsurface inclusions of different shapes. The formulation of the problem in this manner also allows elastic stresses and strains to be determined everywhere in the half-space. In the case of large transformational strains, such as may be associated with the anomalous topography at the TAG hydrothermal field, faulting and fracturing may occur in addition to simple surface deformation and uplift. The pattern of faulting and/or fracturing that might occur is likely to depend on the shape of the inclusion even though the surface uplift may not. Although large-strain and failure-based analyses may provide better constraints on the geometry of the serpentinized region at TAG, we further use the linear elastic model (Sections 2 and 3) to estimate the effect of serpentinization on faulting underneath the TAG region. On the other hand, only relatively small 3% transformational strain increment associated with serpentinization appears to be required to explain uplifts of the Miyazaki Plain and Kyushu Mountains (Figures 3 and 9). For such small strains, the elastic theory presented here is more likely to be adequate.

5.1. Failure Criterion

[46] To first order, the effect of serpentinization on the tendency of the fault to slip could be considered based on the Mohr-Coulomb criterion [e.g., *Jaeger et al.*, 2007]. The simplest approach would be to neglect the effect of the fault itself on the deformation and assume that stress changes resulting from serpentinization develop on the background of existing tectonic stresses. This is similar to describing the tendency of the fault to become unstable as a result of petroleum production [e.g., *Segall and Fitzgerald*, 1998; *Rudnicki*, 1999; *Chanpura and Germanovich*, 2004] where the petroleum reservoir deforms in response to changing pore pressure and causes the stress state to deviate toward or away from failure. Here we use a similar approach considering failure along the identified fault plane or slip zone.

[47] According to the Mohr-Coulomb criterion, the approach of the stress state on a fault plane toward the failure envelope can be described by the Coulomb stress

$$\Delta T = \mathrm{sign}(\tau_0)\Delta\tau_{XY} + (\Delta\sigma_{YY} + \Delta p)\tan\varphi \qquad (15)$$

where τ_0 is the background (initial) tectonic shear stress on the fault plane, $\Delta\tau_{XY}$ and $\Delta\sigma_{YY}$ represent changes of the shear and normal stress components on the fault plane, respectively, Δp is the pore pressure change, and compressive stresses are negative. In all examples below, X- axis is aligned along the long axis of the elliptic inclusion (Figure 5) and is parallel to the fault or slip zone (e.g., Figure 9b). In general, in the normal faulting regime, $\tau_0 < 0$ if $0 \le \theta < \pi/2$ while $\tau_0 > 0$ if $\pi/2 \le \theta < \pi$, where θ is the fault (X-axis) angle in the counter-clock direction with respect to the horizontal (x-axis) ($\theta = \beta$ in Figure 5). The reverse faulting regime is characterized by $\tau_0 > 0$ if $0 \le \theta < \pi/2$ and $\tau_0 < 0$ if $\pi/2 \le \theta < \pi$. This is equivalent to the usual sign convention for shear stress such that it is positive when it gives rise to a couple on the plane in the clockwise direction [e.g., *Timoshenko and Goodier*, 1970]. We assume here that the stress changes do not reverse the fault slip direction, so that the quantity sign $(\tau_0)\Delta\tau_{XY}$ in (15) is positive in the direction of fault slip.

[48] In various forms, the Coulomb stress concept has been employed in many earthquakes studies [e.g., *King et al.*, 1994; *Cocco and Rice*, 2002, 2003; *Smith and Sandwell*, 2003; *Steacy et al.*, 2005; *Ryder et al.*, 2012]. The sign of ΔT characterizes whether the stress state moves closer toward or further away from the failure surface. The stress

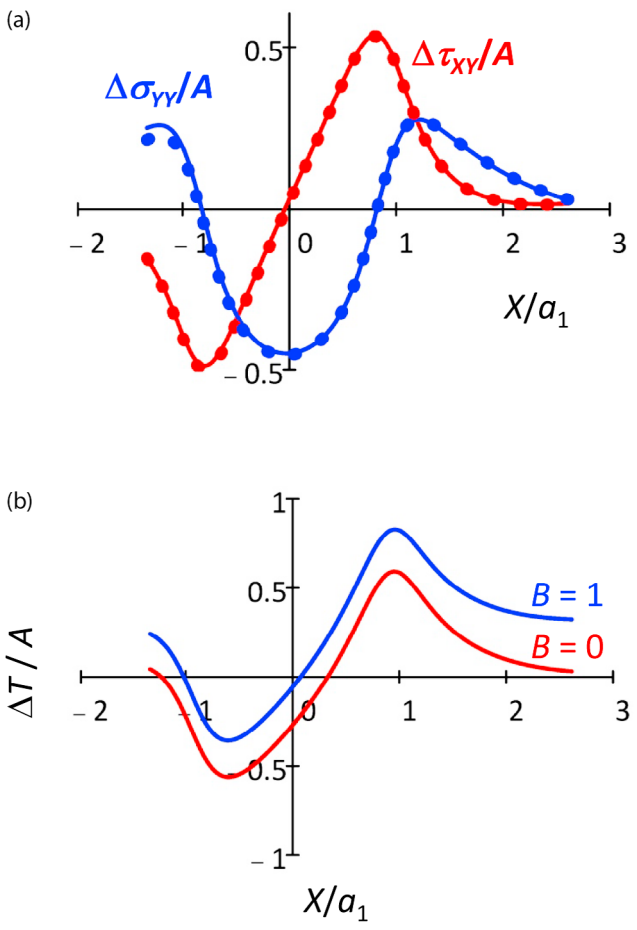

Figure 10. (a) Shear (red lines) and normal (blue lines) stress changes on the slip zone (bold orange dashed line in Figure 9b), which underlies the inclined serpentinized domain (solid blue line in Figure 9b). Stresses are normalized by the mean stress (equation (9)) that would be caused by the same transformation strain inside the same inclusion if it were located in the infinite plane. Solid lines correspond to the case of two inclusions while dotted lines show the stresses along the slip zone without taking into account the sub-horizontal domain. (b) Distribution of the normalized Coulomb stress, $\Delta T/A$, along the slip zone. Skempton coefficients $B = 0$ (red line) and $B = 1$ (blue line) correspond to two limiting cases of the drained and (strongest possible) undrained deformations, respectively. Coordinate X (Figures 5 and 9b) is parallel to the slip zone and normalized by the major semi-axis, a_1, of the inclined ellipse.

change has a tendency to *destabilize* the fault when $\Delta T > 0$. In this case, the stress state moves closer to failure. Note that except for the general information on the nature of the regional stress regime (normal faulting or thrust), ΔT in (15) does not require knowing the initial stresses and only the sign of τ_0 is required. Because (15) reflects stress increments, rather than their absolute values, the Coulomb stress on the pre-existing fault is only affected by the friction angle, while cohesion of the fault material is not present in (15) (as long as it does not change as a result of deformation).

5.2. Serpentinization and Faulting at the Miyazaki Plain Region

[49] The serpentinization of the forearc mantle may have important tectonic implications [e.g., *Hyndman et al.*, 1997; *Seno*, 2005; *Kirby et al.*, 1996]. In particular, *Tahara et al.* [2008] argue that the well-developed serpentinized mantle wedge may be a plausible cause of aseismic slip and relatively low maximum magnitude of events in the Hyuganada region. In the Kyushu-Palau subduction zone, the Philippine Sea Plate converges under the Eurasia Plate, which corresponds to a thrust-type tectonic regime in slip zones (Figure 3a) detected by *Yagi and Kikuchi* [2003]. Along the coastline of eastern Kyushu, the depths of Moho discontinuity and the surface of the subducting slab are about 30 km and 40 km, respectively [e.g., *Tahara et al.*, 2008]. The detected region with high Poisson's ratio (Figure 3) is situated along the upper boundary of the subducting slab [*Tahara et al.*, 2008; *Saiga et al.*, 2010]. In the Kyushu-Palau subduction zone, most of the interplate, thrust-type earthquakes occur near this boundary [*Yagi and Kikuchi*, 2003; *Salah and Seno*, 2008]. Hence, in our simplified model (Figure 9b) of the Miyazaki Plain situation, the slip zone (bold orange dashed line) is located just below the inclined serpentinized inclusion (solid blue line). In general, an inclusion at the hanging wall of a thrust fault (considered in this section) and the Francis's scenario (Figure 1a) of the serpentinization domain at the footwall of a normal fault (considered in Section 5.3) represent two end-members.

[50] Figure 10a shows changes of the normalized shear, $\Delta\tau_{XY}/A$ (red line), and normal, $\Delta\sigma_{YY}/A$ (blue line), stresses on the upper boundary of the subducting Phillipine Sea Plate (or aseismic thrust zone shown by bold orange dashed line in Figure 9b) that underlines the serpentinized domain beneath the Miyazaki Plain (Figure 3). As above, this domain is represented by the inclined elliptic inclusion in Figure 9b, and the axis X of the rotated coordinate set (thin green lines) is parallel to "fault plane" and coincides with the axis of the inclined domain in Figure 9b. The stress distributions in Figure 10a are almost symmetric with respect to $X = 0$ because of the weak interaction with the sub-horizontal serpentinization domain (Figures 3b and 9b) and with the Earth surface, $y = 0$. Dotted lines show the stresses on the same fault (slip zone) in the absence of the sub-horizontal domain. The interaction is weak because the inclined inclusion is relatively deep ($h/a_1 = 1.5$) and because the sub-horizontal inclusion is three-dimensional, so its effect on the stress state decays as the inversed cube of the distance from the inclusion center. This is why in Figure 10a, the dotted lines almost coincide with solid lines (showing stresses when both inclusions are present), which suggests that the effect of the sub-horizontal inclusion on the stress state is indeed small. Figure 10a shows stress distribution in cross-section RR′ (Figure 3a), where the effect of the sub-horizontal inclusion is the strongest. Away from this cross-section, for example along line BB′ in Figure 3a, the interaction between the inclusions is even weaker, so the model of a single 2-D inclined inclusion appears to be adequate. Hereafter, we use the characteristic stress A in equation (9) for normalizing stresses. This is convenient because A is independent of the inclusion dimensions. In addition,

because A is also proportional to ε_0, the normalized stresses in Figures 10a and 10b are independent of the transformation strain.

[51] The distribution of the corresponding normalized Coulomb stress, $\Delta T/A$, on the fault plane is given in Figure 10b. The pressure change Δp in equation (15) was estimated using the Skempton relation for a poroelastic material $\Delta p = -B\Delta I_1/3$ [e.g., *Detournay and Cheng*, 1993], where B is the Skempton coefficient and $\Delta I_1 = \sigma_{xx} + \sigma_{yy} + \sigma_{zz}$ is the first stress invariant. In the case of inclined inclusion, expressions (5), (6), (7), and (11) were used to determine transformation stresses σ_{xx} and σ_{yy}, and the plane strain relation $\sigma_{zz} = \nu(\sigma_{xx} + \sigma_{yy}) - E\varepsilon_0/3$ [e.g., *Timoshenko and Goodier*, 1970] between the stresses was used to evaluate σ_{zz}. The contribution of the sub-horizontal inclusion to ΔI_1 was computed based on the axisymmetric solution of *Mindlin and Cheng* [1950].

[52] In general, the Skempton coefficient B ranges between the thermodynamic bounds of 0 and 1 [*Detournay and Cheng*, 1993]. The case of $B = 0$ (red line in Figure 10b) corresponds to the drained case, when the fluid pressure does not change as the transformation strain is accumulated. The case of $B = 1$ (blue line in Figure 10b) represents another extreme of the (strongest possible) undrained deformation. The limited available data suggests that the Skempton coefficient is in the range of 0.5–0.9 for igneous rocks [*Detournay and Cheng*, 1993]. We are not aware of data for the Skempton coefficient for metamorphic rocks, but in any event, the Skempton relation characterizes the undrained response of the pore pressure to stress changes (unless $B = 0$). It is often used for computing Coulomb stresses in earthquake studies [see, e.g., *Cocco and Rice*, 2002, and reference therein], when the rock loading is relatively fast. For much slower deformational processes associated with serpentinization reactions, one need to evaluate the relative timescales of stress change and pressure dissipation. Although the drained response is probably more realistic, in Figure 10b and further in the paper we present both end-member cases of $B = 0$ and $B = 1$.

[53] Values of the friction coefficient typically used in calculations of the Coulomb stress range between 0.6 and 0.8 [*Cocco and Rice*, 2002]. Because serpentine has a reduced friction coefficient ($\sim$0.2 according to *Escartin et al.* [1997a, 1997b, 2001]), even partially serpentinized material may considerably decrease the friction coefficient in the slip zone. For Figure 10b and below, we used a conservative value 0.7, which is consistent with *Byerlee*'s [1978] law.

[54] As can be observed from Figure 10b, the difference between the Coulomb stresses computed in the drained ($B = 0$) and undrained cases ($B = 1$) is not very significant. In both cases, the stress change, caused by the serpentinization, is favorable for fault slip and seismic events approximately at $X > 0$ (the coordinate set is shown in Figures 5 and 9b) where $\Delta T > 0$. The positive sign of the shear stress change in Figure 10a (red line) is consistent with the thrust-typetectonic shear stresses near the aseismic slip zone in the Kyushu-Palau subduction zone (blue line in Figure 8). At approximately $X > 0$, $\Delta T < 0$, and the stress changes are not favorable for thrust-type events in this part of the slip zone. Therefore, our results indicate a possibility of serpentinization-related strengthening ($\Delta T < 0$) of the slip zone $X < 0$ below the central part of the serpentinized domain where the slip zone "touches" the serpentinized domain. Above this place, there is a tendency for serpentinization-enhanced weakening ($\Delta T < 0$ and $\Delta\tau_{XY} > 0$) of a significant part $X > 0$ of the slip zone.

[55] It is important to emphasize that the faulting and fracturing activity in slip zones may be related to other subduction processes rather than to serpentinization of the mantle wedge. Also, we computed Coulomb stresses on a specified plane of the potential slip. Instead, Coulomb stress changes can be computed on optimally orientated planes, which presumes that the faults with highest ΔT will be most likely to slip [e.g., *King et al.*, 1994]. The elongated inclined inclusion (Figures 3 and 9) generates tensile stress changes in the surrounding material in the direction parallel to its long axis and compressive stress changes in the perpendicular direction. Because of a relatively mild inclusion inclination (25°), this corresponds to promoting normal-fault events in the region below the serpentined domain. This is consistent with seismic observations of *Tahara et al.* [2008] who note that intraplate earthquakes associated with normal faulting occur in the Hyuganada region beneath where serpentinization may be occurring.

5.3. Effect of Serpentinization on Normal Faulting

[56] *Francis* [1981] proposed several scenarios of the effect of serpentinization on faulting. In the case of normal faulting, he suggested that, rocks beneath the footwall of a normal fault hydrate as a result of seawater infiltrating down the fault, so that serpentinization occurs generating more movement on the fault and uplift (Figure 1a). To quantify this scenario, we consider its simplified version when a circular, serpentinized inclusion is located at the footwall of a normal fault (Figure 11a). Shear (black dotted line), normal (green dashed line) and Coulomb (solid lines) stresses, normalized by A, are shown in Figure 11b. The stresses are plotted along the part of the normal fault shown in Figure 11a by the red dashed line. In general, above the serpentinized domain, Coulomb stress on the fault is positive whereas the shear stress is negative (Figure 11b). The latter is consistent with the direction of slip on a normal fault. Consequently, the serpentinization process would tend to enhance the slip on this part of the fault, and, in turn, fault slip may enhance the access of water required for the serpentinization reactions.

5.4. Serpentinization and Detachment at TAG

[57] We note again that the small-strain elastic consideration such as in Figures 10 and 11 is only applicable to small transformation strains, probably, no more than a few percent. This is why we do not consider here larger strains such as expected in the TAG region (Section 4.2) and for which large-strain elastic or inelastic considerations would be more appropriate. Instead we consider an increment, $\Delta\varepsilon_0$, of the transformation strain on the background transformation strain, ε_0, that may be happening beneath the TAG field. Assuming that small $\Delta\varepsilon_0$ causes small stress increments, we treat them as being elastic and employ equations (5)–(11), where we replace ε_0 with $\Delta\varepsilon_0$.

[58] Figure 12a shows a simple model of serpentinization at the footwall of a TAG-like detachment fault. We use the same geometry of the elliptical inclusion as in Figure 7b.

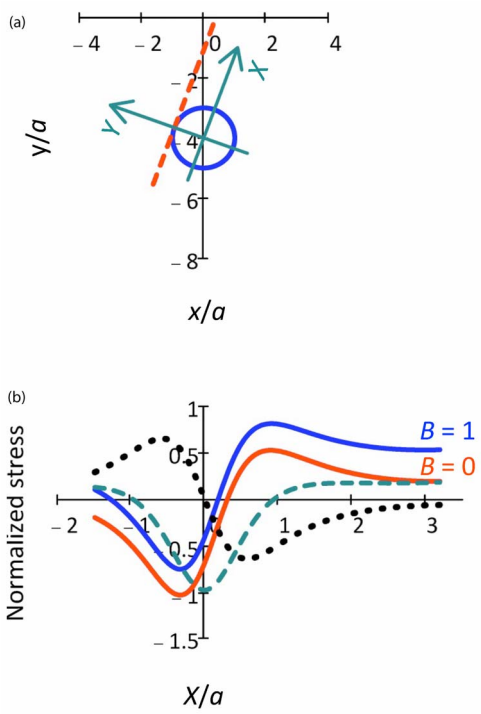

Figure 11. (a) A model of *Francis*'s [1981] scenario of serpentinization domain (blue line) at the footwall of a normal fault (Figure 1a). Both vertical and horizontal coordinates are normalized by the radius, a, of the circular inclusion. Coordinate set X, Y is shown by the green lines with X-axis parallel to the fault (red dashed line). (b) Coulomb (blue, $B = 1$, and red, $B = 0$, solid lines), shear (black dotted line), and normal (green dashed line) stresses (normalized by A) along the fault plane shown in Figure 11a.

That is, the inclusion center is at the depth of $h = 1.6$ km and its axes are $2a = 4$ km and $2b = 0.8$ km. As discussed in Section 4.2, massive serpentinization ($\varepsilon_0 \approx 40\%$) in the 3-D elastic domain is required to cause the observed uplift at TAG (Figure 2). Here we consider a 2-D inclusion, elongated horizontally along the detachment fault, and analyze the possible effect of serpentinization on both the detachment fault and on normal faults that are typically associated with detachment faults [e.g., *Buck*, 1988; *Lister et al.*, 1986] and appear to be present at the TAG area [*deMartin*, 2007]. Examples of such normal faults are shown in Figure 12a by three parallel lines inclined at the angle of $\theta = 70°$ to the horizontal and connecting the seafloor with the detachment fault. We ignore the effects of the irregularities caused by the faults at the seafloor.

[59] In the extreme case of the strongest Skempton effect ($B = 1$), Coulomb stresses (not shown in Figure 12b) are positive on all three normal faults. Shear stresses (solid lines in Figure 12b) are negative everywhere on the normal faults. Hence, the serpentinization would tend to bring the faults closer to failure because the negative sign of shear stresses is consistent with slip direction on the normal fault ($\tau_0 < 0$ for $0 \le \theta < \pi/2$). In another extreme case, Skempton coefficient $B = 0$. Then, Coulomb stresses (dashed lines in Figure 12b) may become negative on deeper normal faults, but are still positive on the shallowest normal fault shown on the right in Figure 12a. A real situation would be somewhere in between, although $B = 0$ is probably more realistic for TAG conditions.

[60] This analysis indicates that serpentinization in a relatively shallow domain at the footwall of a detachment fault tends to enhance the permeability of some overlying normal faults (Figure 12a) and the detachment fault itself. Hence, normal faulting may provide pathways for water needed for serpentinization reactions. Similar computations for the detachment fault suggest that for entire range of the Skempton coefficient ($0 \le B \le 1$), serpentinization tends to enhance the slip on the detachment fault above the upper half of the serpentinized inclusion (see also *Francis*'s [1981] and scenario in Figure 11). This is why shallower normal faults (such as the normal fault on the right in Figure 12a) and the

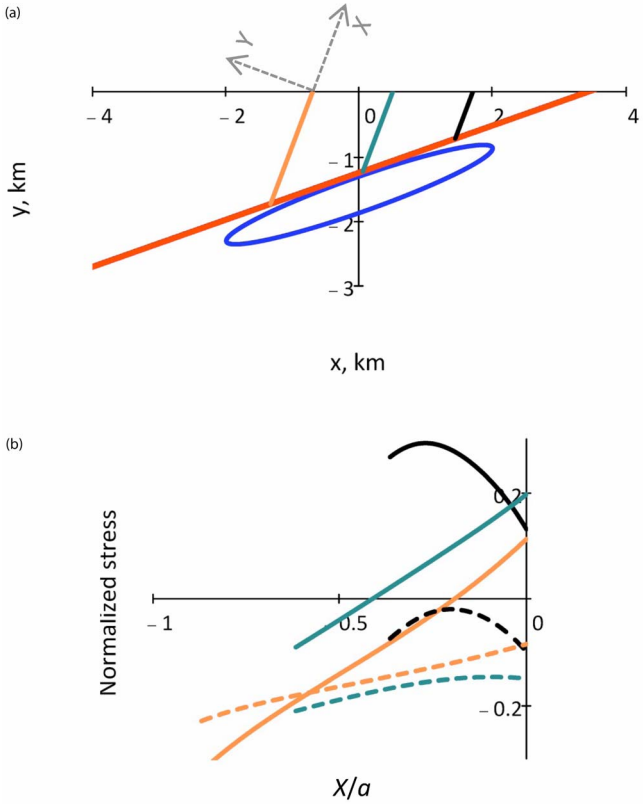

Figure 12. (a) A 2-D model of elliptical serpentinization domain (blue line) at the footwall of the TAG detachment fault (red line) and three representative cases of normal faults (orange, green, and black lines inclined at 70° to the horizontal) associated with the detachment fault. The inclusion is located at the depth of $h = 1.6$ km and has axes of $2a = 4$ km and $2b = 0.8$ km. (b) Coulomb (solid lines) and shear (dashed lines) stresses (normalized by A) on the normal faults that shown in Figure 12a by lines of the same colors. Orange, green, and black lines correspond to the left, middle, and right faults in Figure 12a, respectively. Calculations were done for both $B = 1$ and $B = 0$, but only the results for drained conditions ($B = 0$), which is probably more realistic for TAG, are shown. Shear stress is independent of B. For each normal fault, coordinate X (gray dashed line) is directed along the fault plane with its zero being on the seafloor.

detachment fault itself may be important water pathways for keeping the serpentinization process going.

[61] Our model also suggests that serpentinization at TAG promotes slip on the deep normal fault (not shown in Figure 12a), which accommodates the lithospheric extension and may be focusing deep hydrothermal fluids [*deMartin et al.*, 2007]. The lithospheric extension is also accommodated on two antithetic normal faults [*deMartin et al.*, 2007, Figure 2b], but the serpentinization-induced shear is not consistent with normal faulting and is not likely to enhance the slip on these faults.

6. Discussion

6.1. Effects of Depth and Shape of Serpentinized Domain on Seafloor Uplift

[62] While interior displacements caused by a point dilation source differ from those due to a spherical inclusion in the elastic half-space, the surface displacements are identical and expressions (3) give the exact solution for both cases. Similarly, solution (4) for the surface displacement caused by the circular (cylindrical) inclusion is the same as that for the 2-D point (line) source in the elastic half plane. Hence, as far as the surface uplift is concerned, both spherical and circular cylindrical inclusions in the half-space can be represented by a point source (3-D or 2-D, respectively) regardless of their depth. This is not the case for inclusions of other shapes.

[63] When the inclusion depth, h, is of the order of its size, $2a$, or greater, the resulting surface uplift is relatively insensitive to the shape and orientation of inclusions with the same volume (Section 4.1). In general, it is well known that asymptotic solutions may be applicable even when asymptotic parameters are not necessarily small or large. In particular, this has been observed in solutions for surface subsidence caused by horizontal tunnels [*Pinto and Whittle*, 2006; *Puzrin et al.*, 2012], for surface uplift caused by a pressurized magma chamber [*Segall*, 2010], and for fractures interacting with a body boundary [e.g., *Dyskin et al.*, 2000]. For example, *McTigue* [1987] considers a pressurized, spherical magma chamber in an elastic half-space and represents the surface uplift as a series of powers of a/h, where a is the chamber radius and h is its depth. The leading-order term in his expression for the surface uplift is proportional to $(a/h)^3$ and recovers *Mogi*'s [1958] point dilatation model. The second, higher order term accounts for the cavity size, but this correction is rather weak, of the order of $(a/h)^6$. This result allowed *McTigue*'s [1987] to explain why *Mogi*'s [1958] approach works reasonably well even when a/h is close to 1.

[64] A similar argument applies for the stress-strain state perturbed by the inclusion considered in this work. For example, when $a^2 - b^2 \ll h^2$, the fraction term in (14) is small, so (12) can be written as

$$u(x,0) + iw(x,0) = 2ab\frac{\varepsilon_0(1+\nu)}{3}\frac{x+ih}{x^2+h^2} \cdot \left[1 + \frac{e^{-2i\beta}(a^2-b^2)}{4}\frac{(x+ih)^2}{(x^2+h^2)^2} + O(\varepsilon^4)\right] \tag{16}$$

where $\varepsilon = (a^2 - b^2)^{1/2}/h$ and $O(\varepsilon^4)$ indicates the omitted terms of the higher order. The leading-order terms for the vertical and horizontal surface displacements in (16) are $O(\varepsilon^2)$ and $O(\varepsilon)$, respectively. The second term in (16) provides corrections for the inclusion shape and depth that are of the order of $O(\varepsilon^2)$ and $O(\varepsilon^4)$, respectively. Hence, in both cases the correction is two orders higher in the powers of ε. For all computations in this work we used the exact solution (13) rather than its asymptotic expansion (16). The latter helps, however, to show why the source solution (4) works well even when ε is not considerably smaller than one.

[65] In 3-D, the difference between the point-source solution [*Mindlin and Cheng*, 1950; *Mogi*, 1958] and its main correction is *three* orders [*McTigue*'s, 1987] rather than two orders (in powers of ε) in 2-D. Hence, the effect of the free surface and inclusion shape is weaker in three-dimensional geometries than in two-dimensional. We used this observation in Sections 4.2, 4.3, and 5.2.

[66] Currently, the existence of serpentinized mantle associated with the subduction of the oceanic crust is inferred from seismic tomography data [*Salah and Seno*, 2008; *Hyndman and Peacock*, 2003] such as the downdip limit of interplate thrust earthquakes [e.g., *Hyndman et al.*, 1997], intraslab earthquakes within the crust part of the subducting slab [e.g., *Seno*, 2005], low-frequency tremors in the forearc [*Seno and Yamasaki*, 2003; *Matsubara et al.*, 2008], and from the V_p/V_s ratio obtained by seismic tomography [*Salah and Seno*, 2008; *Tahara et al.*, 2008]. Our results indicate that uplift data may provide an additional constraint on inferring serpentinization from geological and seismological observations.

6.2. Tensile Fracturing

[67] Based on the *Eshelby* [e.g., *Jaswon and Bhargava*, 1961] or *Mindlin and Cheng* [1950] solutions among others, it is expected that tensile stresses could be generated in the material surrounding a dilating body. Tensile stresses may induce or enhance tensile fracturing in rock because typically tensile strength of rocks is relatively low [e.g., *Jaeger et al.*, 2007]. In the context of this work, tensile fractures could enhance rock permeability providing better water access to the serpentinizing body. As an example, we evaluate the stress state near the seafloor. Because at or near the free surface, σ_{yy} and τ_{xy} stress components are zero or small due to the boundary conditions, we concentrate on the normal stress σ_{xx}.

[68] This stress can be easily computed using the exact solution (13). To simplify analysis, however, we follow the above consideration for displacements, and consider a deep inclusion. Similar to (17), when $a^2 - b^2 \ll h^2$, equation (18) can be written as

$$\sigma_{xx}(x) = \frac{16\varepsilon_0(1+\nu)\mu}{3\pi(\kappa+1)}S\frac{h^2-x^2}{(h^2+x^2)^2}[1+O(\varepsilon^2)] \tag{17}$$

where $S = \pi ab$ is the domain cross-sectional area and the small parameter $\varepsilon = (a^2 - b^2)^{1/2}/h$ is the same as in (16). Expression (17) can also be obtained by the integration of the *Mindlin and Cheng* [1950] 3-D source solution and represents its 2-D equivalent. Numerical comparison of (17) and (13) shows that in general, asymptotic expression (17) deviates considerably from the exact solution (13) only when the inclusion depth becomes smaller than its size.

[69] We see from (17) that $\sigma_{xx} > 0$ (i.e., tensile) if $-h < x < h$. In other words, the volumetric extension in a relatively deep (i.e., $a^2 - b^2 \ll h^2$) serpentinization domain may

promote tensile fracturing on or near the seafloor just above the domain and regardless of its shape. We note that *Karson and Rona* [1990] and *Bohnenstiehl and Kleinrock* [2000] observed open fissures on the ocean floor in the vicinity of the active hydrothermal mound at the TAG area. While not necessarily created by the serpentinization transformation strain, location of the fissure zone is consistent with our results. Indeed, the fissure zone is located on the hanging wall of the detachment fault and above the possible serpentinization domain inferred by *Palmer* [1996] and *deMartin et al.* [2007] from vent chemistry and seismic observations.

6.3. Fluid Flow and Heat Transfer

[70] The exothermic character of serpentinization reactions [*Fyfe and Londsale*, 1981; *Macdonald and Fyfe*, 1985] and the chemical signatures associated with serpentinization reactions [*Janecky and Seyfried*, 1986; *Berndt et al.*, 1996; *Allen and Seyfried*, 2004] may provide controls on both physical and biogeochemical aspects of seafloor hydrothermal activity. This is especially relevant at slow-spreading ridges where the magma budget is low [*Lowell and Rona*, 2002; *Rona*, 2008].

[71] The models described here do not include the dynamical processes of fluid and heat transfer associated with large scale serpentinization. As a result of volume expansion associated with serpentinization, permeable pathways may tend to close. However, as transformational strains grow, the stresses generated are likely to generate new permeable pathways for fluid to access fresh rock. This may be especially relevant when serpentinization occurs near an active fault such as the detachment fault at TAG or Atlantis Massif [*Boschi et al.*, 2006].

[72] To obtain a rough estimate of the rate of serpentinization and the potential for exothermic heat release to impact hydrothermal temperatures, we consider the results for the topographic salient at TAG discussed in Section 4.2. The rate of serpentinization $\dot{M}$ is given by

$$\dot{M} \sim \rho_r V \phi / t \tag{18}$$

where $\rho_r \approx 2500$ kg/m^3 is the density of serpentine, V is the volume of the body undergoing serpentinization, ϕ is the fraction of the body that has been serpentinized, and t is the time over which reaction occurs. For example, if the TAG salient (Figure 2) is the result of serpentinization of ≈40% of a 25 km^3 volume over 10^5 years (here, $\phi = 40\%$ corresponds to $\varepsilon_0 \approx 20\%$ in Figure 7), expression (18) results in $\dot{M} \approx 10$ kg/s. Following *Lowell and Rona* [2002], the temperature change ΔT_s associated with serpentinization during hydrothermal flow can be determined approximately from the heat balance expression

$$\Delta T_s = \frac{\gamma \dot{M}}{c_f Q + c_f Q_s + c_r \dot{M}} \tag{19}$$

where γ is the latent heat released during serpentinization, Q is the total hydrothermal mass flow through the system, $Q_s \sim 0.1\dot{M}$ (see below) is the mass inflow of water absorbed in the serpentinization reaction to support the rate $\dot{M}$, and c_f and c_r are the specific heats of the fluid and rock respectively. The hydrothermal heat flux at TAG is approximately 1700 MW [*Wichers et al.*, 2005] and with a mean black smoker temperature of 365°C [*Rona et al.*, 1993], this results in a mass flow rate $Q \approx 930$ Kg/s. Substituting this value of Q into equation (19) along with values of γ and specific heats from Table 1 shows that the temperature increase resulting from serpentinization is <1°C. The small transformation (thermoelastic) strains that would be associated with these small temperature changes are negligible compared with the strains associated with the serpentinization process itself. The domed salient or projection in the east wall of the axial valley beneath the most active part of the TAG hydrothermal field occurs in the hanging wall of the detachment fault zone above a serpentinized body inferred to occur beneath the underlying footwall (Figures 2 and 12a). The small scale of this feature suggests that it is not likely a result of flexure of the lithosphere, nor does the salient appear to be a volcanic construct.

[73] The solution for the uplift of the Miyazaki Plain is dominated by the two-dimensional, inclined inclusion with the area undergoing serpentinization of $\pi a_1 b_1$=1885 km^2 (Figure 9). In this case, $\phi \approx 6\%$ of the region is serpentinized over 1.2×10^5 years ($\phi = 6\%$ corresponds to $\varepsilon_0 \approx 3\%$ in Figure 9). Assuming that the third dimension is at least $L \sim 100$ km and using equation (18) to estimate the rate of serpentinization, we obtain $\dot{M} \approx 8 \times 10^3$ kg/s. Therefore, the rate of serpentinization at the Miyazaki Plain site is significantly greater than that at TAG. This is because the volume undergoing serpentinization is much greater than at TAG. The specific serpentinization rate (per rock unit volume) scales as $\dot{M}/V \sim \rho_r \phi / t$, however, and this rate appears to be much greater for TAG ($\sim 10^{-2}$ kg/(m^{3}yr)) than for Miyazaki Plain ($\sim 10^{-3}$ kg/(m^{3}yr)). The strain and surface uplift associated with the heat release from serpentinization is therefore negligible compared with the transformation strain resulting from serpentinization.

[74] If we assume that approximately 1 mol of H_2O is required to serpentinize each mole of peridotite [*O'Hanley*, 1992], the rate $\dot{M} = 8 \times 10^3$ kg/s would require a mass flow $Q_s \approx 10^3$ kg/s (i.e., $Q_s \sim 0.1\ \dot{M}$). Presumably this water flux could be provided by dewatering of the subducting slab [*Hyndman et al.*, 1997]. Because the throughput of fluid beneath the Miyazaki plain is unknown we provide an upper estimate of the thermal effect of serpentinization by assuming that the all available water is consumed in the serpentinizations reactions. This results in $Q = 0$ in equation (19), which then suggests that the latent heat release would raise the temperature of serpentinized rock by about $\gamma/(c_r + 0.1c_f) \approx 270$°C. Incrementally serpentinizing ≈6% of the material beneath the Miyazaki Plain would result in $\Delta T_s \approx 16$°C. For a characteristic value $\alpha \sim 10^{-5}$ 1/°C of the coefficient of thermal expansion, the corresponding volumetric strain of thermal expansion is $\alpha \Delta T_s \approx 0.02\%$. This is significantly smaller than the transformation strain of $\Delta\varepsilon_0 = 3\%$ that corresponds to the 6% of the serpentinized material. In addition, because the rate of serpentinization per unit volume at the Miyazaki Plain is smaller than at TAG, its effect on the thermal regime is also likely to be small. While we recognize that there may be other factors contributing to the uplift, this result may provide an important constraint for modeling the interplay between the serpentinization and the water cycle in subduction zones [e.g., *Rüpke et al.*, 2004].

7. Conclusions

[75] In this paper, we calculated the transformation strain associated with spherically, cylindrically, and elliptically

shaped inclusions in an elastic half-space to determine the resulting crustal deformation, stress change, and surface uplift. We showed that if the normalized depth, $h/(2a)$ of the inclusion was greater than ≈0.75, the resulting surface uplift was relatively insensitive to the shape and orientation of inclusions with the same volume.

[76] Application of the results to explain the anomalous salient that extends 3.5 km westward from the east wall of the axial valley at the TAG hydrothermal field suggests that this feature may result from a serpentinized body at depth beneath the footwall of a detachment fault. Because the depth of the potential serpentinized region beneath the TAG hydrothermal field appears to be more than the inclusion size, the uplift profile is relatively insensitive to the exact shape of the serpentinized domain. Approximately 20% to 40% transformational strain is required to generate the observed uplift. Cracking associated with the expansion produced by the inferred serpentinization should generate a distinctive microseismic signature, which could be identifiable in the abundant ongoing microseismicity recorded in the TAG area [*deMartin et al.*, 2007]. The rate of exothermic heat release needed to produce the serpentinized volume over $\sim 10^5$ years is too small to significantly impact hydrothermal heat output at the TAG mound, except perhaps in the Low Temperature Zone (Figure 2) where it may contribute to ongoing diffuse flow.

[77] Application of the results to an uplift feature associated with the Kyushu-Palau subduction zone in the western Pacific suggests that approximately 3% transformational strain in an elliptically shaped serpentinized region of the mantle wedge near the subducted Kyushu-Palau Ridge may result in the observed uplift on the Miyazaki Plain. The rate of serpentinization needed to produce the uplift is $\approx 8 \times 10^3$ kg/s, yielding fluid mass transfer rate of $\approx 10^3$ kg/s.

[78] Transformation strain affects the stress field in and around the region undergoing serpentinization. Our analysis, based on the Coulomb stress approach, suggests that serpentinization at the footwall of a normal fault [*Francis*, 1981] tends to enhance fault slip and, in turn, fault slip may enhance the access of water required for the serpentinization reactions. Serpentinization of a region beneath the footwall of the TAG detachment fault tends to enhance the slip along some overlying normal faults, which may then result in fluid pathways to the deeper crust to continue the serpentinization process and maintain the overlying hydrothermal system. Depending upon location, serpentinization at the hanging wall of a thrust fault, may result in serpentinization-related strengthening or weakening. Transformational strains associated with serpentinization underneath the Miyazaki Plain may promote thrust-type events in the aseismic slip zone near the upper boundary of the subducting Philippine Sea Plate.

Appendix A: Displacements in a Half-Space Caused by Cylindrical Inclusion

[79] The plain-strain distribution of dimensionless vertical, w, and horizontal, u, displacements in half plane $y < 0$ with circular (cylindrical) inclusion (Figure 4a) are given by

$$\begin{cases} \dfrac{w}{a} = \dfrac{2\varepsilon_0(1+\nu)}{3(\kappa+1)}\left\{-\dfrac{\eta+\eta_0}{R_1^m} + \dfrac{\kappa(\eta-\eta_0)}{R_2^2} - \dfrac{2\eta[\xi^2-(\eta-\eta_0)^2]}{R_2^4}\right\} \\ \dfrac{u}{a} = \dfrac{2\varepsilon_0(1+\nu)}{3(\kappa+1)}\left\{\dfrac{\xi}{R_1^m} + \dfrac{\kappa\xi}{R_2^2} - \dfrac{4\xi\eta(\eta-\eta_0)}{R_2^4}\right\} \end{cases} \tag{A1}$$

where $R_1 = \sqrt{\xi^2+(\eta+\eta_0)^2}$, $R_2 = \sqrt{\xi^2+(\eta-\eta_0)^2}$, $m = 1$ and $m = 0$ in the inclusion exterior ($R_1 > 1$) and interior ($R_1 < 1$), respectively, $\xi = x/a$ and $\eta = y/a$ are the normalized, rectangular coordinates, and $\eta_0 = h/a$ is the dimensionless depth of the inclusion. Expressions (A1) are obtained as a particular case of *Ru*'s [1999] solution for an elliptical inclusion in half plane (see also Appendix B) and agree with a more general solution for two adjacent half planes with different elastic properties and a thermal, circular [*Aderogba and Berry*, 1971] or elliptical [*Ru et al.*, 2001] inclusion in one of them. Substituting $\eta = 0$ in (A1), we have the distribution (4) of surface displacements. Note that in this appendix, parameters with dimension of length are normalized by the inclusion radius, a. This is different from the main text and, in particular, from expressions (4), where such parameters are normalized by the inclusion depth, h.

Appendix B: Displacements in a Half-Space With Inclined Elliptic Inclusions

[80] We use equation (7) with equation (5) to obtain displacements:

$$u + iw = -\frac{2\kappa\varepsilon_0}{\kappa+1}\frac{1+\nu}{3} \cdot \left\{\overline{D(\bar{z})} - \overline{P(\bar{z})} + D(\bar{z}) - P(\bar{z}) - (z-\bar{z})[D'(\bar{z}) - P'(\bar{z})]\right\} \tag{B1}$$

This expression simplifies for the surface points where $y = 0$ and $z = \bar{z} = x$:

$$u + iw = (2/3)\varepsilon_0(1+\nu)^{-1}[\overline{D(x)} - \overline{P(x)}] \quad (y = 0) \tag{B2}$$

[81] To find functions $D(z)$ and $P(z)$, we follow *Ru* [1999] and write conformal mapping $\omega(\varsigma)$ in equations (6)–(8) as finite sum of $N + 2$ terms:

$$z = \omega(\zeta) = \lambda\zeta + z_0 + \sum_{k=1}^{N}\frac{c_k}{\zeta^k} \tag{B3}$$

where $\zeta = \omega^{-1}(z)$, z_0 is a point located inside inclusion and designated as the inclusion "center," and λ, c_1, c_2, … are complex coefficients. Choosing $\omega(\varsigma)$ in this form allows treating many practically important inclusion shapes [e.g., *Savin*, 1970; *Muskhelishvili*, 1979]. Substituting $\zeta = \omega^{-1}(z)$ in equation (B3) and the result in equation (8) gives

$$D(z) = \frac{\bar{\lambda}}{\zeta} + \bar{z}_0 + \sum_{k=1}^{N} \bar{c}_k \zeta^k, \quad \zeta = \omega^{-1}(z) \tag{B4}$$

Because on the boundary, $|\zeta| = 1$, of the unit circle, $\bar{\zeta} = 1/\zeta$, on the inclusion boundary, $z = \omega(\zeta) = \omega(1/\bar{\zeta}) = \omega(1/\overline{\omega^{-1}(z)})$. Therefore, function $D(z)$, defined by (8), satisfies condition $D(z) = \bar{z}$ on the inclusion boundary. *Ru* [1999] used this condition to express *two* unknown stress functions through *one* auxiliary function $D(z)$ (equations (6) and (7)). To find $P(z)$, recall that this is the polynomial part of $D(z)$ at infinity, where $D(z)$ has a pole of degree N and can be represented as

$$D(z) = \sum_{n=-\infty}^{N} a_n z^n \tag{B5}$$

Here a_1, a_2, … are complex coefficients that are determined by substituting (B3) in (B5) and comparing coefficients for different powers of ζ. Equations (B3) and (B4) only slightly differ from those studied by *Ru* [1999] in the case of a real coefficient λ. Using complex λ enables convenient consideration of an inclined elliptical inclusion.

[82] In the case of inclined elliptical inclusion, $N = 1$, $\lambda = e^{i\beta}(a + b)/2$, $c_1 = e^{i\beta}(a - b)/2$, and (B4) reduces to

$$D(z) = \frac{\bar{\lambda}}{\omega^{-1}(z)} + \bar{z}_0 + \bar{c}_1 \omega^{-1}(z) \tag{B6}$$

which is equivalent to $D(z)$ in (11) when $z_0 = -ih$ is the coordinate of the inclusion center.

[83] As follows from the second equation in (10), or directly from (B3),

$$\omega^{-1}(z) = (z - ih)/\lambda + O(1/z) \quad (z \to \infty) \tag{B7}$$

Hence, per equation (8), $D(z)$ behaves at infinity as

$$D(z) = \overline{z_0} + \frac{\overline{c_1}}{\lambda}(z - z_0) + O\left(\frac{1}{z}\right) \quad (z \to \infty) \tag{B8}$$

and the polynomial $P(z)$ with the same behavior at $z \to \infty$ is defined by

$$P(z) = \overline{z_0} + \frac{\overline{c_1}}{\lambda}(z - z_0) \tag{B9}$$

This expression is identical to $P(z)$ in (11) for $z_0 = -ih$.

[84] Substituting equations (B6) and (B7) into equation (B2), and taking into account that on the half plane boundary $\bar{z} = z = x$, results in

$$u(x,0) + iw(x,0) = \frac{4ab}{3(a^2 - b^2)} \varepsilon_0 (1 + \nu) e^{2i\beta} (x - \bar{z}_0) \cdot \left[1 - \sqrt{1 - \frac{e^{-2i\beta}(a^2 - b^2)}{(x - \bar{z}_0)^2}}\right] \tag{B10}$$

which is identical to (12), (14) when $z_0 = -ih$ (Figure 5).

[85] Similar to (B2), stresses at the half plane surface $y = 0$ can be obtained by substituting $z = \bar{z} = x$ in (5)–(7):

$$\sigma_{xx}(x,0) = \frac{8\mu}{3(\kappa + 1)} \varepsilon_0 (1 + \nu)[D'(x) - P'(x) + \overline{D'(x)} - \overline{P'(x)}],$$
$$\sigma_{yy}(x,0) = 0, \quad \tau_{xy}(x,0) = 0 \tag{B11}$$

where

$$D'(z) - P'(z) = -\frac{2ab}{(z - z_0)^2} \cdot \left[1 - \frac{e^{2i\beta}(a^2 - b^2)}{(z - z_0)^2} + \sqrt{1 - \frac{e^{2i\beta}(a^2 - b^2)}{(z - z_0)^2}}\right]^{-1} \tag{B12}$$

Second and third expressions in (B11) simply show that the boundary conditions on the half plane boundary $y = 0$ are satisfied, but the first one results in (13) when $z_0 = -ih$.

[86] **Acknowledgments.** We thank the Associate Editor David W. Sparks and Donna Blackman for their insightful comments on the original version of this manuscript. We are grateful to Michitaka Tahara and Atsushi Saiga for sending us high resolution versions of their figures in *Tahara et al.* [2008] and *Saiga et al.* [2010], which helped to produce Figures 3a and 3b of this paper, respectively. This work was supported in part under NSF Grants OCE 1131355 to LNG and OCE 1131471 to RPL.

References

Aderogba, K. V., and D. S. Berry (1971), Inclusions in a two-phase elastic space-plane circular and rectangular inclusions, *J. Mech. Phys. Solids*, *19*, 285–293, doi:10.1016/0022-5096(71)90014-7.

Agrinier, P., G. Cornen, and M. O. Beslier (1997), Mineralogical, and oxygen isotopic features of serpentinites recovered from the ocean/continent transition in the Iberia Abyssal Plain, *Proc. Ocean Drill. Program, Sci. Results*, *149*, 541–552.

Allen, D. E., and W. E. Seyfried (2004), Serpentinization and heat generation: Constarints from Lost City and Rainbow hydrothermal systems, *Geochim. Cosmochim. Acta*, *68*, 1347–1354, doi:10.1016/j.gca.2003.09.003.

Berndt, M. E., D. E. Allen, and W. E. Seyfried Jr. (1996), Reduction of CO_2 during serpentinization of olivine at 300° C and 500 bar, *Geology*, *24*, 351–354, doi:10.1130/0091-7613(1996)024<0351:ROCDSO>2.3.CO;2.

Blackman, D. K., et al. (2002), Geology of the Atlantis Massif (Mid-Atlantic Ridge, 30 degrees N): Implications for the evolution of an ultramafic oceanic core complex, *Mar. Geophys. Res.*, *23*, 443–469, doi:10.1023/B:MARI.0000018232.14085.75.

Bohnenstiehl, D., and M. Kleinrock (2000), Fissuring near the TAG active hydrothermal mound, 26°N on the Mid-Atlantic Ridge, *J. Volcanol. Geotherm. Res.*, *98*(1–4), 33–48, doi:10.1016/S0377-0273(99)00192-4.

Bonatti, E. (1976), Serpentinite protrusions in the oceanic crust, *Earth Planet. Sci. Lett.*, *32*, 107–113, doi:10.1016/0012-821X(76)90048-0.

Bonatti, E., and P. R. Hamlyn (1981), Oceanic ultramafic rocks, in *The Sea*, vol. 7, edited by C. Emiliani, pp. 241–283, John Wiley, New York.

Boschi, C., G. L. Früh-Green, A. Delacour, J. A. Karson, and D. S. Kelley (2006), Mass transfer and fluid flow during detachment faulting and development of an oceanic core complex, Atlantis Massif (MAR 30°N), *Geochem. Geophys. Geosyst.*, *7*, Q01004, doi:10.1029/2005GC001074.

Bougault, H., J. L. Charlou, Y. Fouquet, H. D. Needham, N. Vaslet, P. Appriou, P. J. Baptiste, P. A. Rona, L. Dmitriev, and S. Silantiev (1993), Fast and slow spreading ridges: Structure and hydrothermal activity, ultramafic topographic highs, and CH_4 output, *J. Geophys. Res.*, *98*(B6), 9643–9651, doi:10.1029/93JB00508.

Buck, W. R. (1988), Flexural rotation of normal faults, *Tectonics*, *7*(5), 959–973, doi:10.1029/TC007i005p00959.

Byerlee, J. (1978), Friction of rocks, *Pure Appl. Geophys.*, *116*(4), 615–626, doi:10.1007/BF00876528.

Canales, J. P., R. A. Sohn, and B. J. deMartin (2007), Crustal structure of the Trans-Atlantic Geotraverse (TAG) segment (Mid-Atlantic Ridge, 26°10′N): Implications for the nature of hydrothermal circulation

and detachment faulting at slow-spreading ridges, *Geochem. Geophys. Geosyst.*, *8*, Q08004, doi:10.1029/2007GC001629.

Cann, J. R., D. K. Blackman, D. K. Smith, E. McAllister, B. Janssen, S. Mello, E. Averinos, A. R. Pascoe, and J. Escartin (1997), Corrugated slip surfaces formed at ridge-transform intersections on the Mid-Atlantic Ridge, *Nature*, *385*, 329–332, doi:10.1038/385329a0.

Cannat, M. (1993), Emplacement of mantle rocks in the sea floor at mid-ocean ridges, *J. Geophys. Res.*, *98*, 4163–4172, doi:10.1029/92JB02221.

Cannat, M., D. Bideau, and H. Bougalt (1992), Serpentinized peridotites and gabbros in the Mid-Atlantic Ridge axial valley at 15°37′N and 16°52′N, *Earth Planet. Sci. Lett.*, *109*, 87–106, doi:10.1016/0012-821X(92)90076-8.

Cannat, M., et al. (1995), Thin crust, ultramafic exposures, and rugged faulting patterns at the Mid-Atlantic Ridge (22°–24°N), *Geology*, *23*, 49–52, doi:10.1130/0091-7613(1995)023<0049:TCUEAR>2.3.CO;2.

Cannat, M., Y. Lagebrielle, H. Bougault, J. Casey, N. de Coutures, L. Dmitriev, and Y. Fouquet (1997), Ultramafic and gabbroic exposures at the Mid-Atlantic Ridge: Geological mapping in the 15°N region, *Tectonophysics*, *279*, 193–213, doi:10.1016/S0040-1951(97)00113-3.

Carlson, R. L., and D. J. Miller (1997), A new assessment of the abundance of serpentinite in the oceanic crust, *Geophys. Res. Lett.*, *24*, 457–460, doi:10.1029/97GL00144.

Chanpura, R. A., and L. N. Germanovich (2004), Fault stability inside and near a depleting petroleum reservoir, in *Gulf Rocks 2004, Proceedings of the 6th North America Rock Mechanics Symposium (NARMS), June 5–9, 2004, Houston, Texas*, pp. 1–12, Am. Rock Mech. Assoc., Alexandria, Va.

Cocco, M., and J. R. Rice (2002), Pore pressure and poroelasticity effects in Coulomb stress analysis of earthquake interactions, *J. Geophys. Res.*, *107*(B2), 2030, doi:10.1029/2000JB000138.

Cocco, M., and J. R. Rice (2003), Correction to "Pore pressure and poroelasticity effects in Coulomb stress analysis of earthquake interactions" by Massimo Cocco and James R. Rice, *J. Geophys. Res.*, *108*(B2), 2069, doi:10.1029/2002JB002319.

Coleman, R. G. (1971), Petrologic and geophysical nature of serpentinites, *Geol. Soc. Am. Bull.*, *82*, 897–918, doi:10.1130/0016-7606(1971)82[897:PAGNOS]2.0.CO;2.

Davies, J. H. (2003), Elastic field in a semi-infinite solid due to thermal expansion or a coherently misfitting inclusion, *J. Appl. Mech.*, *70*, 655–660.

deMartin, B. J. (2007), Experimental and seismological constraints on the rheology, evolution, and alteration of the lithosphere at oceanic spreading centers, PhD thesis, Mass. Inst. of Technol. Woods Hole Oceanogr. Inst. Joint Program, Boston.

deMartin, B. J., R. A. Sohn, J. P. Canales, and S. E. Humphris (2007), Kinematics and geometry of active detachment faulting beneath the Trans-Atlantic Geotraverse (TAG) hydrothermal field on the Mid-Atlantic Ridge, *Geology*, *35*, 711–714, doi:10.1130/G23718A.1.

Detournay, E., and A. H. D. Cheng (1993), Fundamentals of poroelasticity, in *Comprehensive Rock Engineering*, vol. 2, edited by J. Hudson, chap. 5, pp. 113–169, Pergamon, Oxford, U. K.

Dick, H. J. B. (1989), Abyssal peridotites, very slow spreading ridges and ocean ridge magmatism, in *Magmatism in the Ocean Basin*, edited by A. D. Saunders and M. J. Norry, *Geol. Soc. Spec. Publ.*, *42*, 71–105, doi:10.1144/GSL.SP.1989.042.01.06.

Dyskin, A., L. Germanovich, and K. Ustinov (2000), Asymptotic analysis of crack interaction with free boundary, *Int. J. Solids Struct.*, *37*(6), 857–886, doi:10.1016/S0020-7683(99)00063-3.

Dziak, R. P., C. G. Fox, R. W. Embley, J. L. Nabelek, J. Braunmiller, and R. A. Koski (2000), Recent tectonics of the Blanco ridge, Eastern Blanco Transform Fault zone, *Mar. Geophys. Res.*, *21*, 423–450, doi:10.1023/A:1026545910893.

Escartin, J., and M. Cannat (1999), Ultramafic exposures and the gravity signature of the lithosphere near the Fifteen-Twenty Fracture Zone (Mid-Atlantic Ridge, 14°–16.5°N), *Earth Planet. Sci. Lett.*, *171*, 411–424, doi:10.1016/S0012-821X(99)00169-7.

Escartin, J., G. Hirth, and B. Evans (1997a), Nondilatant brittle deformation of serpentinites: Implications for Mohr-Coulomb theory and the strength of faults, *J. Geophys. Res.*, *102*(B2), 2897–2913, doi:10.1029/96JB02792.

Escartin, J., G. Hirth, and B. Evans (1997b), Effects of serpentinization on the lithospheric strength and the style of normal faulting at slow-spreading ridges, *Earth Planet. Sci. Lett.*, *151*(3), 181–189, doi:10.1016/S0012-821X(97)81847-X.

Escartin, J., G. Hirth, and B. Evans (2001), Strength of slightly serpentinized peridotites: Implications for the tectonics of oceanic lithosphere, *Geology*, *29*, 1023, doi:10.1130/0091-7613(2001)029<1023:SOSSPI>2.0.CO;2.

Faccenda, M., L. Burlini, T. V. Gerya, and D. Mainprice (2008), Fault-induced seismic anisotropy by hydration in subducting oceanic plates, *Nature*, *455*(7216), 1097–1100, doi:10.1038/nature07376.

Francis, T. J. G. (1981), Serpentinization faults and their role in the tectonics of slow spreading ridges, *J. Geophys. Res.*, *86*, 11,616–11,622, doi:10.1029/JB086iB12p11616.

Früh-Green, G. L., A. Plas, and C. Lecuyer (1996), Petrologic and stable isotope constraints on hydrothermal alteration and serpentinization of the EPR shallow mantle at Hess Deep (site 895), *Proc. Ocean Drill. Program, Sci. Results*, *147*, 255–291.

Fryer, P. (1996a), Evolution of the Mariana convergent plate margin system, *Rev. Geophys.*, *34*, 89–125, doi:10.1029/95RG03476.

Fryer, P. (1996b), An actively venting serpentine seamount on the southeastern Mariana forearc: "Shinkai 6500" Dives 280 and 281, *Jamstec J. Deep Sea Res.*, *12*, 247–256.

Fryer, P., and M. J. Mottl (1992), Lithology, mineralogy, and origin of serpentine muds recovered from Conical and Torishima forearc seamounts: Results from Leg 135 drilling, *Proc. Ocean Drill. Program, Sci. Results*, *125*, 343–362.

Fyfe, W. S., and P. Londsale (1981), Ocean floor hydrothermal activity, in *The Sea*, vol. 7, *The Oceanic Lithosphere*, edited by C. Emiliani, pp. 589–638, John Wiley, New York.

Gillis, K., et al. (1993), *Proceedings of the Ocean Drilling Program Initial Reports*, vol. 147, 366 pp., Ocean Drill. Program, College Station, Tex.

Goodier, J. N. (1937), On the integration of the thermo-elastic equations, *Philos. Mag.*, *23*, 1017–1032.

Hilairet, N., and B. Reynard (2009), Stability and dynamics of serpentinite layer in subduction zone, *Tectonophysics*, *465*, 24–29, doi:10.1016/j.tecto.2008.10.005.

Hirauchi, K., I. Katayama, S. Uehara, M. Miyahara, and Y. Takai (2010), Inhibition of subduction thrust earthquakes by low-temperature plastic flow in serpentine, *Earth Planet. Sci. Lett.*, *295*, 349–357, doi:10.1016/j.epsl.2010.04.007.

Hyndman, R. D., and S. M. Peacock (2003), Serpentinization of the forearc mantle, *Earth Planet. Sci. Lett.*, *212*(3–4), 417–432, doi:10.1016/S0012-821X(03)00263-2.

Hyndman, R. D., K. Wang, and M. Yamano (1995), Thermal constraints on the seismogenic portion of southwestern Japan subduction thrust, *J. Geophys. Res.*, *100*, 15,373–15,392, doi:10.1029/95JB00153.

Hyndman, R. D., M. Yamano, and D. A. Oleskevitch (1997), The seismogenic zone of subduction thrust faults, *Isl. Arc*, *6*, 244–260, doi:10.1111/j.1440-1738.1997.tb00175.x.

Ildefonse, B., D. K. Blackman, B. E. John, Y. Ohara, D. J. Miller, and C. J. MacLeod (2007), Oceanic core complexes and crustal accretion at slow-spreading ridges, *Geology*, *35*, 623–626, doi:10.1130/G23531A.1.

Jaeger, J. C., N. G. W. Cook, and R. W. Zimmerman (2007), *Fundamentals of Rock Mechanics*, 4th ed., 475 pp., Blackwell, Oxford, U. K.

Janecky, D. R., and W. E. Seyfried Jr. (1986), Hydrothermal serpentinization of peridotite within the oceanic crust: Experimental investigations of mineralogy and major element chemistry, *Geochim. Cosmochim. Acta*, *50*, 1357–1378, doi:10.1016/0016-7037(86)90311-X.

Jaswon, M. A., and R. D. Bhargava (1961), Two-dimensional elastic inclusion problems, *Proc. Cambridge Philos. Soc.*, *57*, 669–680, doi:10.1017/S0305004100035702.

Kamata, H., and K. Kodama (1999), Volcanic history and tectonics of the southwest Japan arc, *Isl. Arc*, *8*(3), 393–403, doi:10.1046/j.1440-1738.1999.00241.x.

Karson, J. A., and R. M. Lawrence (1997), Tectonic setting of serpentinite exposures on the western median valley wall of the MARK Area in the vicinity of Site 920, *Proc. Ocean Drill. Program. Sci. Results*, *153*, 5–21.

Karson, J. A., and P. A. Rona (1990), Block-tilting, transfer faults, and structural control of magmatic and hydrothermal processes in the TAG area, Mid-Atlantic Ridge 26°N, *Geol. Soc. Am. Bull.*, *102*, 1635–1645, doi:10.1130/0016-7606(1990)102<1635:BTTFAS>2.3.CO;2.

King, G. C. P., R. S. Stein, and J. Lin (1994), Static stress changes and the triggering of earthquakes, *Bull. Seismol. Soc. Am.*, *84*(3), 935–953.

Kirby, S., E. R. Engdahl, and R. Denlinger (1996), Intermediate-depth intraslab earthquakes and arc volcanism as physical expressions of crustal and uppermost mantle metamorphism in subducting slabs, in *Subduction Top to Bottom*, *Geophys. Monogr. Ser.*, vol. 96, edited by E. Bebout et al., pp. 195–214, AGU, Washington, D. C., doi:10.1029/GM096p0195.

Lalou, C., J. L. Reyss, E. Brichet, P. A. Rona, and G. Thompson (1995), Hydrothermal activity on a 10^5-year scale at a slow-spreading ridge: TAG area, Mid-Atlantic Ridge, *J. Geophys. Res.*, *100*, 17,855–17,862, doi:10.1029/95JB01858.

Lister, G. S., M. A. Etheridge, and P. A. Symonds (1986), Detachment faulting and the evolution of passive continental margins, *Geology*, *14*(3), 246–250, doi:10.1130/0091-7613(1986)14<246:DFATEO>2.0.CO;2.

Lowell, R. P., and P. A. Rona (2002), Seafloor hydrothermal systems driven by sepentinization of peridotite, *Geophys. Res. Lett.*, *29*(11), 1531, doi:10.1029/2001GL014411.

Macdonald, A. H., and W. S. Fyfe (1985), Rate of serpentinization in seafloor environments, *Tectonophysics*, *116*, 123–135, doi:10.1016/0040-1951(85)90225-2.

MacLeod, C. J., R. C. Searle, B. J. Murton, J. F. Casey, C. Mallows, S. C. Unsworth, K. L. Achenbach, and M. Harris (2009), Life cycle of oceanic core complexes, *Earth Planet. Sci. Lett.*, *287*, 333–344, doi:10.1016/j.epsl.2009.08.016.

Matsubara, M., K. Obara, and K. Kasahara (2008), Three-dimensional P- and S-wave velocity structures beneath the Japan Islands obtained by high-density seismic stations by seismic tomography, *Tectonophysics*, *454*(1–4), 86–103, doi:10.1016/j.tecto.2008.04.016.

Mavko, G., T. Mukerji, and J. Dvorkin (2003), *The Rock Physics Handbook: Tools for Seismic Analysis of Porous Media*, Cambridge Univ. Press, Cambridge, U. K.

McTigue, D. (1987), Elastic stress and deformation near a finite spherical magma body: Resolution of the point source paradox, *J. Geophys. Res.*, *92*(B12), 12,931–12,940, doi:10.1029/JB092iB12p12931.

Mével, C. (2003), Serpentinization of abyssal peridotites at mid-ocean ridges, *C. R. Geosci.*, *335*, 825–852, doi:10.1016/j.crte.2003.08.006.

Mével, C., and C. Stamoudi (1996), Hydrothermal alteration of the upper-mantle sections at Hess Deep, *Proc. Ocean Drill. Program, Sci. Results*, *147*, 293–309.

Mindlin, R. D., and D. H. Cheng (1950), Thermoelastic stress in the semi-infinite solid, *J. Appl. Phys.*, *21*, 931–933, doi:10.1063/1.1699786.

Miranda, E. A., and Y. Dilek (2010), Oceanic core complex development in modern and ancient oceanic lithosphere: Gabbro-localized versus peridotite-localized detachment models, *J. Geol.*, *118*, 95–109, doi:10.1086/648460.

Mogi, K. (1958), Relations between the eruptions of various volcanoes and the deformations of the ground surfaces around them, *Bull. Earthquake Res. Inst.*, *36*, 99–134.

Mottl, M. J., S. C. Komor, P. Fryer, and C. L. Moyer (2003), Deep-slab fuel extremophilic Archaea on a Mariana forearc serpentinite mud volcano: Ocean Drilling Program Leg 195, *Geochem. Geophys. Geosyst.*, *4*(11), 9009, doi:10.1029/2003GC000588.

Muskhelishvili, N. I. (1979), *Some Basic Problems of the Mathematical Theory of Elasticity*, 768 pp., Noordhoff, Leyden, Netherlands.

Nagaoka, S., H. Maemoku, and Y. Matsushima (1991), Evolution of Holocene coastal landforms in the Miyazaki Plain, Southern Japan, *Quat. Res.*, *30*, 59–78.

Nakada, M., M. Tahara, H. Shimizu, S. Nagaoka, K. Uehira, and S. Suzuki (2002), Late Pleistocene crustal uplift and gravity anomaly in the eastern part of Kyushu, Japan, and its geophysical implications, *Tectonophysics*, *351*, 263–283, doi:10.1016/S0040-1951(02)00161-0.

Nicolas, A. (1989), *Structure of Ophiolite and Dynamics of Ocean Lithosphere*, 367 pp., Kluwer Acad., Dordrecht, Netherlands, doi:10.1007/978-94-009-2374-4.

Nowacki, W. (1986), *Thermo-Elasticity*, 2nd ed., Pergamon, Oxford, U. K.

O'Hanley, D. S. (1992), Solution to the volume problem in serpentinization, *Geology*, *20*, 705–708, doi:10.1130/0091-7613(1992)020<0705:STTVPI>2.3.CO;2.

Palmer, M. R. (1996), Hydration and uplift of the oceanic crust on the Mid-Atlantic Ridge associated with hydrothermal activity: Evidence from boron isotopes, *Geophys. Res. Lett.*, *23*, 3479–3482, doi:10.1029/96GL02079.

Pinto, F., and A. Whittle (2006), Discussion of "Elastic solution for tunneling-induced ground movements in clays" by K. H. Park, *Int. J. Geomech.*, *6*, 72–73, doi:10.1061/(ASCE)1532-3641(2006)6:1(72).

Puzrin, A. M., J. B. Burland, and J. R. Standing (2012), Simple approach to predicting ground displacements caused by tunnelling in undrained anisotropic elastic soil, *Geotechnique*, *62*(4), 341–352, doi:10.1680/geot.10.P.127.

Reston, T. J. (2009), The structure, evolution, and symmetry of the magma-poor rifted margins of the North and Central Atlantic: A synthesis, *Tectonophysics*, *468*, 6–27, doi:10.1016/j.tecto.2008.09.002.

Rona, P. A. (2008), The changing vision of marine minerals, *Ore Geol. Rev.*, *33*, 618–666, doi:10.1016/j.oregeorev.2007.03.006.

Rona, P. A., L. Widenfalk, and K. Bostrom (1987), Serpentinized ultramafics and hydrothermal activity at the Mid-Atlantic Ridge crest near 15°N, *J. Geophys. Res.*, *92*(B2), 1417–1427, doi:10.1029/JB092iB02p01417.

Rona, P. A., M. D. Hannington, C. V. Raman, and G. Thompson (1993), Active and relict seafloor hydrothermal mineralization at the TAG hydrothermal field, Mid-Atlantic Ridge, *Econ. Geol.*, *88*, 1989–2017, doi:10.2113/gsecongeo.88.8.1989.

Ru, C. Q. (1999), Analytic solution for Eshelby's problem of an inclusion of arbitrary shape in a plane and half-plane, *J. Appl. Mech.*, *66*, 315–322, doi:10.1115/1.2791051.

Ru, C. Q., P. Schiavone, and A. Mioduchowski (2001), Elastic fields in two jointed half-planes with an inclusion of arbitrary shape, *ZAMP*, *52*, 18–32, doi:10.1007/PL00001538.

Rudnicki, J. W. (1999), Alteration of regional stress by reservoirs and other inhomogeneities: Stabilizing or destabilizing?, in *Proceedings of the 9th International Congress on Rock Mechanics*, vol. 3, edited by G. Vouille and P. Berest, pp. 1629–1637, Taylor & Francis, New York.

Rüpke, L. H., J. P. Morgan, M. Hort, and J. A. D. Connolly (2004), Serpentine and the subduction zone water cycle, *Earth Planet. Sci. Lett.*, *223*, 17–34, doi:10.1016/j.epsl.2004.04.018.

Ryder, I., A. Rietbrock, K. Kelson, R. Bürgmann, M. Floyd, A. Socquet, C. Vigny, and D. Carrizo (2012), Large extensional aftershocks in the continental forearc triggered by the 2010 Maule earthquake, Chile, *Geophys. J. Int.*, *1365*(246), 879–890, doi:10.1111/2011.05321.

Saiga, A., S. Matsumoto, K. Uehira, T. Matsushima, and H. Shimizu (2010), Velocity structure in the crust beneath the Kyushu area, *Earth Planets Space*, *62*(5), 449–462, doi:10.5047/eps.2010.02.003.

Salah, M. K., and T. Seno (2008), Imaging V_p, V_s, and Poisson's ratio anomalies beneath Kyushu, southwest Japan: Implications for volcanism and forearc mantle wedge serpentinization, *J. Asian Earth Sci.*, *31*, 404–428, doi:10.1016/j.jseaes.2007.07.003.

Savin, G. N. (1970), Stress distribution around holes, *NASA Tech. Transl.*, *NASA TT F-607*, 997 pp.

Segall, P. (2010), *Earthquake and Volcano Deformation*, Princeton Univ. Press, Princeton, N. J.

Segall, P., and S. D. Fitzgerald (1998), A note on induced stress changes in hydrocarbon and geothermal reservoirs, *Tectonophysics*, *289*, 117–128, doi:10.1016/S0040-1951(97)00311-9.

Seno, T. (2005), Variation of downdip limit of the seismogenic zone near the Japanese islands: Implications for the serpentinization mechanism of the forearc mantle wedge, *Earth Planet. Sci. Lett.*, *231*(3–4), 249–262, doi:10.1016/j.epsl.2004.12.027.

Seno, T., and S. Maruyama (1984), Paleographic reconstruction and origin of the Philippine Sea, *Tectonophysics*, *102*, 53–84, doi:10.1016/0040-1951(84)90008-8.

Seno, T., and T. Yamasaki (2003), Low-frequency tremors, intraslab and interplate earthquakes in Southwest Japan—From a viewpoint of slab dehydration, *Geophys. Res. Lett.*, *30*(22), 2171, doi:10.1029/2003GL018349.

Shimoyama, S., H. Kinoshita, M. Miyahara, Y. Tanaka, T. Ichihara, and K. Takemura (1999), Mode of vertical crustal movements during the Late Quaternary in Kyushu, Japan, deduced from heights of ancient shorelines, *Tectonophysics*, *302*, 9–22, doi:10.1016/S0040-1951(98)00280-7.

Skelton, A., and M. Jakobsson (2007), Could peridotite hydration reactions have provided a contributory driving force for Cenozoic uplift and accelerated subsidence along the margins of the North Atlantic and Labrador Sea?, *Norweg. J. Geol.*, *87*, 21–28.

Smith, B., and D. Sandwell (2003), Coulomb stress accumulation along the San Andreas Fault system, *J. Geophys. Res.*, *108*(B6), 2296, doi:10.1029/2002JB002136.

Steacy, S., S. S. Nalbant, J. McCloskey, C. Nostro, O. Scotti, and D. Baumont (2005), Onto what planes should Coulomb stress perturbations be resolved?, *J. Geophys. Res.*, *110*, B05S15, doi:10.1029/2004JB003356.

Tahara, M., K. Uehira, H. Shimizu, M. Nakada, T. Yamada, K. Mochizuki, M. Shinohara, M. Nishino, R. Hino, and H. Yakiwara (2008), Seismic velocity structure around the Hyuganada region, Southwest Japan, derived from seismic tomography using land and OBS data and its implications for interplate coupling and vertical crustal uplift, *Phys. Earth Planet. Inter.*, *167*, 19–33, doi:10.1016/j.pepi.2008.02.001.

Timoshenko, S. P., and J. N. Goodier (1970), *Theory of Elasticity*, 3rd ed., McGraw-Hill, New York.

Tucholke, B. E., and J. Lin (1994), A geological model for the structure of ridge segments in slow-spreading ocean crust, *J. Geophys. Res.*, *99*(B6), 11,937–11,958, doi:10.1029/94JB00338.

Tucholke, B. E., J. Lin, and M. C. Kleinrock (1998), Megamullions and mullion structure defining oceanic metamorphic core complexes on the mid-Atlantic ridge, *J. Geophys. Res.*, *103*, 9857–9866, doi:10.1029/98JB00167.

Wheat, C. G., P. Fryer, A. T. Fischer, S. Hulme, H. Jannasch, M. J. Mottl, and K. Becker (2008), Borehole observations of fluid flow from South Chamorro Seamount, an active serpentinite mud volcano in the Mariana forearc, *Earth Planet. Sci. Lett.*, *267*, 401–409, doi:10.1016/j.epsl.2007.11.057.

Wichers, S., R. Reves-Sohn, and G. Terray (2005), New constraints on the thermal power of the TAG hydrothermal system and the dynamics of the water column plume, *Eos Trans. AGU*, *86*(52), Fall Meet. Suppl., Abstract OS33A-1466.

Yagi, Y., and M. Kikuchi (2003), Partitioning between seismogenic and aseismic slip as highlighted from slow slip events in Hyuga-nada, Japan, *Geophys. Res. Lett.*, *30*(2), 1087, doi:10.1029/2002GL015664.

Zonenshain, L. P., M. I. Kuzmin, A. P. Lisitsin, Y. A. Bogdanov, and B. V. Baranov (1989), Tectonics of the Mid-Atlantic rift-valley between the TAG and MARK areas (26–24-degrees-N) — Evidence for vertical tectonism, *Tectonophysics*, *159*, 1–23, doi:10.1016/0040-1951(89)90167-4.